The Institute for Solid State Physics
The University of Tokyo

Activity Report 2011

ISSP

Activity Report 2011

Contents

	Pages
Preface	1
Research Highlights	2 - 33
Highlights of Joint Research	34 - 51
ISSP Workshops	52 - 55
Subjects of Joint Research	56 - 125
Publications	126 - 162

Preface

This booklet constitutes the annual Activity Report of the Institute for Solid State Physics (ISSP), the University of Tokyo for the academic year 2011.

The massive earthquake and tsunami on March 11 devastated the Pacific coast area of the northeastern region of Japan. The accident of the Fukushima nuclear plant aggravated the situation. Our life and research activity were profoundly affected by the disaster. Fortunately, the damage incurred by the facilities and equipments in Kashiwa Campus was relatively small. By contrast, those at the neutron facilities in Tokai (J-PARC and JRR-3) and the synchrotron radiation facility (Photon Factory) in Tsukuba were rather severe. Nonetheless, thanks to dedicated efforts by the staff, recovery process was smooth and rapid. At the time of this writing, most of the facilities are back in operation, except that JRR-3 is still waiting for clearance of regulation tightened after the Fukushima nuclear plant accident.

Notable developments in the past year and those in progress are the following:

(1) Inauguration of the Center of Computational Materials Science -- This new research center launched in April 2011 acts as the headquarter of the Computational Materials Science Initiative (CMSI), an all-Japan organization of computational materials scientists to promote research using the advanced computational resorces including the K-supercomputer.

(2) Progress in ultrahigh magnetic field project -- Two frontiers of high magnetic field generation are pursued in the International MegaGauss Science Laboratory. The non-destructive long-pulse magnet project, which utilizes combination of a capacitance bank and a dc motor generator with flywheel as the power source. Efforts towards development of magnet coil systems are underway. For the destructive ultrahigh magnetic field project, upgrading of the large capacitance bank system for electromagnetic compression method, recently granted by the MEXT is in progress.

(3) New phase of photon science in ISSP -- The Division of Advanced Spectroscopy and the Synchrotron Radiation Laboratory will be reorganized into a new research center, provisionally called Center of Coherent Photon Science, which aims at extending the horizon of spectroscopy and photon science based on remarkable progress in light sources currently underway. Emphases will be laid upon advancing the frontier of laser photoelectron spectroscopy towards ever shorter wavelength regime and implementation of cutting-edge spectroscopic techniques using synchrotron radiation light at the BL07LSU of SPring-8 and X-FEL beam in Harima.

The academic year 2012 is the third of the 6 year term (from 2010 to 2015) granted to the Joint-Usage/Research Centers such as ISSP. Accordingly, ISSP is to go through a mid-term evaluation process by the MEXT. Since the communication with and contribution to the research community are the key of joint usage/research activity, we would welcome opinions and suggestions from various viewpoints of researchers.

May, 2012

Yasuhiro Iye
Director
Institute for Solid State Physics
The University of Tokyo

A Heterogeneous Spin State in Volborthite with a Distorted Kagomé Lattice

Takigawa and Hiroi Groups

The spin-1/2 antiferromagnetic Heisenberg model on a kagomé lattice, a two dimensional network of corner-sharing equilateral triangles, is a theoretical paradigm to look for exotic spin liquid without symmetry breaking. Materials in real world, however, always deviate from the ideal model due, for example, to anisotropy, longer range interactions, lattice distortion, or disorder, which often lead to different kinds of symmetry breaking. This is by itself a very interesting issue, allowing us to understand novel mechanisms of various quantum phase transitions.

Vorlborthite $Cu_3V_2O_7(OH)_2{\cdot}2H_2O$ has distorted kagomé layers formed by isosceles triangles, and hence two Cu sites, Cu1 and Cu2. It shows a sequence of magnetization steps, indicating field-induced phase transitions [1]. We have performed ^{51}V NMR experiments on a high quality powder sample at various magnetic fields [2-4]. The phase diagram obtained from our work is shown in Fig. 1(a). At low fields below 4.5 T, a magnetic transition near 1 K is evidenced by broadening of the NMR line and a peak in nuclear relaxation rates $1/T_1$ and $1/T_2$. However, the ordered phase (phase I) is anomalous with non-uniform magnitude of ordered moment and dense low energy excitations [2].

A second ordered phase (phase II) appears above 4.5 T, where the first magnetization step occurs. A remarkable feature of phase II is the existence of two types of V sites, V_f and V_s sites. Although their NMR spectra overlap as shown in Fig. 1(b), they are clearly distinguished by different spin-echo decay rates $1/T_2$, the V_f (V_s) site showing fast (slow) decay, and distinct line shapes. This indicates spontaneous emergence of two types of Cu sites with distinct dynamics, which form a heterogeneous superstructure.

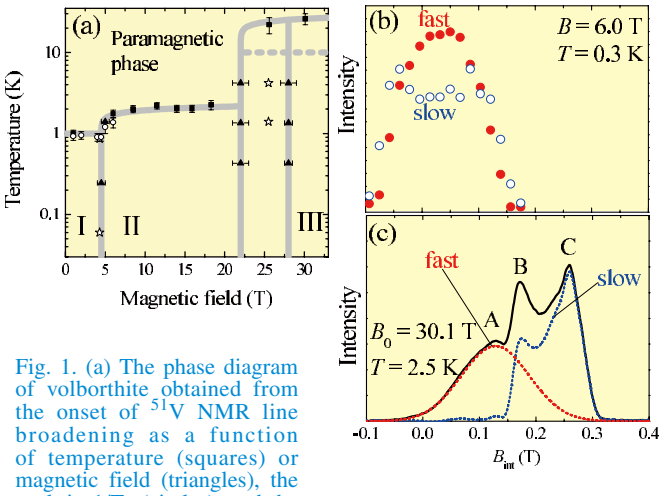

Fig. 1. (a) The phase diagram of volborthite obtained from the onset of ^{51}V NMR line broadening as a function of temperature (squares) or magnetic field (triangles), the peak in $1/T_1$ (circles), and the magnetization steps (stars). The lines are guide to the eyes. The transition between phases II and III are broadened probably due to anisotropy of g-value in a powder sample. (b) The NMR spectrum in phase II decomposed into contributions from the fast (V_f) and slowly (V_s) decaying V sites. (c) The NMR spectrum in phase III again decomposed into the V_f and V_s sites. The large shift at the V_s site indicates ferromagnetic alignment of a part of the Cu spins, which are strongly coupled to the V_s sites.

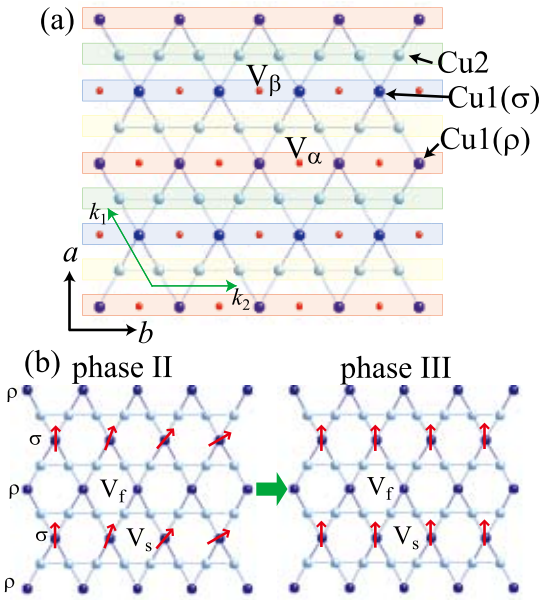

Fig. 2. Possible magnetic structures in volborthite projected onto the a–b plane. (a) Superstructure along the k_1 direction provides two inequivalent V sites, V_f and Vs, and three inequivalent Cu sites, Cu1(σ), Cu1(ρ), and Cu2. (b) If the coupling tensors are largely isotropic and have similar magnitudes, different relaxation behavior at the V_f and V_s sites should be ascribed to the distinct spin states at the Cu1(σ), and Cu1(ρ) sites.

In phase III two distinct V sites still exist and now their spectra are clearly separated (Fig. 1c). A large internal field at the V_s site indicates a large magnetization for a part of the Cu spins, which are strongly coupled to the V_s site and provides a natural explanation for the second magnetization step, which occurs between phase II and III.

Based on these observations, we propose the spin structures of phase II and III (Fig. 2). The two types of V sites naturally suggest two types of Cu1 sites, one with modulated moments and large fluctuations and the other with a fixed magnitude of moment and less fluctuations. They form a spontaneous superstructure. The second magnetization step is then associated with the ferromagnetic saturation of the latter. This scenario is partially consistent with theories for the anisotropic kagome antiferromagnet in the limit of strong interaction within 1D Cu2 chains coupled by weak and frustrated interaction through Cu1 sites.

References

[1] H. Yoshida, Y. Okamoto, T. Tayama, T. Sakakibara, M. Yokunaga, A. Matsuo, Y. Narumi, K. Kindo, M. Yoshida, M. Takigawa, and Z. Hiroi, J. Phys. Soc. Jpn. **78**, 043704 (2009).

[2] M. Yoshida, M. Takigawa, H. Yoshida, Y. Okamoto, and Z. Hiroi, Phys. Rev. Lett. **103**, 077207 (2009).

[3] M. Yoshida, M. Takigawa, H. Yoshida, Y. Okamoto, and Z. Hiroi, Phys. Rev. B **84**, 020410(R) (2011).
[4] M. Yoshida, M. Takigawa, S. Krämer, S. Mukhopadhyay, M. Horvatić, C. Berthier, H. Yoshida, Y. Okamoto, and Z. Hiroi, J. Phys. Soc. Jpn. **81**, 024703 (2012).

Authors
M. Yoshida, M. Takigawa, S. Krämer, S. Mukhopadhyay, M. Horvatić, C. Berthier, H. Yoshida, Y. Okamoto, and Z. Hiroi

Superconducting Gap Structure of $CeIrIn_5$ from Field-Angle-Resolved Measurements of its Specific Heat

Sakakibara Group

The heavy-fermion systems CeMIn$_5$ (M = Co, Rh, and Ir) have been extensively studied because they exhibit unconventional superconductivity near the antiferromagnetic (AF) quantum critical point. Recently, field-angle-resolved specific heat $C(\phi)$ experiments along with the theoretical works have confirmed that $CeCoIn_5$ is a $d_{x^2-y^2}$-wave superconductor [1], and its pairing interaction is widely accepted to be AF spin fluctuations. Similarly, from the $C(\phi)$ experiment, pressure induced superconductivity in $CeRhIn_5$ is argued to have the same pairing symmetry [2]. By contrast, the gap structure of $CeIrIn_5$ (T_c = 0.4 K) has remained controversial. While the $d_{x^2-y^2}$-wave gap was supported from the field-angle-resolved thermal conductivity measurements [3], the gap function k_z or $k_z(k_x+ik_y)$, both of which have a horizontal line node only on the equator and are in sharp contrast to the $d_{x^2-y^2}$-wave gap, was suggested from the effect of impurity scattering on the thermal conductivity [4]. In order to settle the controversy over the gap structure of $CeIrIn_5$, we have performed $C(\phi)$ measurements down to 80 mK [5].

Figure 1(a) shows the specific heat measured in magnetic field H rotated in the tetragonal ab plane. A clear fourfold oscillation was observed with maxima in fields along the <110> direction at 110 mK and 0.2 T. To characterize the H and T variations of the fourfold oscillation, we fit the data to the expression $C_0(T) + C_H(T, H)(1 - A_4\cos 4\phi)$ and show the contour plot of $A_4(T, H)$ in Fig. 1(b). Here, C_0 and C_H are the zero-field and field-dependent components of the electronic specific heat, respectively, and A_4 is the amplitude of the fourfold oscillation normalized by C_H. We found that $A_4(T, H)$ exhibits a peak at around $0.3T_c$ and $0.15H_{c2}$, and rapidly decreases down to zero around $0.2T_c$. This observed feature can be well reproduced by the microscopical calculations assuming the $d_{x^2-y^2}$-wave gap.

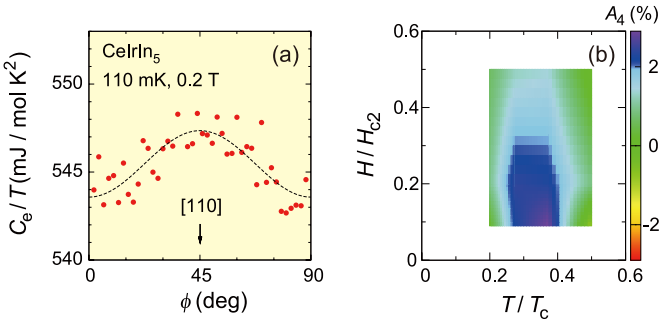

Fig. 1. (a) Variations of the specific heat as a function of the azimuthal angle ϕ between the [100] axis and the magnetic field applied in the ab plane. (b) A contour plot of the normalized fourfold amplitude $A_4(T, H)$ of $CeIrIn_5$.

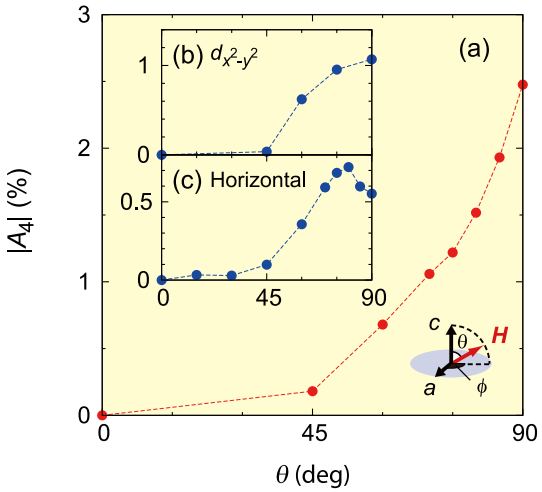

Fig. 2. (a) Polar angle θ dependence of A_4 obtained by conically rotating magnetic field with the strength of $0.2H_{c2}(\theta)$ at 110 mK. Calculated θ dependence of A_4 for (b) the $d_{x^2-y^2}$-wave gap and (c) the horizontal line node gap. The observed monotonic variation of A_4 with θ confirms the absence of a horizontal line node on the equator and strongly supports the $d_{x^2-y^2}$-wave gap.

However, as claimed in Ref. [4], the ϕ rotation experiment alone cannot rule out the possibility of the horizontal line node. In order to solve this issue, we investigated $C(\phi)$ by conically rotating H at several fixed θ, where θ denotes the polar angle between H and the c axis. As shown in Fig. 2(a), A4 is monotonically suppressed by tilting H out of the ab plane. According to the microscopical calculations, a gradual and monotonic decrease of A_4 on decreasing θ from 90 deg is expected for the $d_{x^2-y^2}$-wave gap (Fig. 2(b)), whereas $A_4(\theta)$ is predicted to have a dip around θ =90 deg for the horizontal line node gap (Fig. 2(c)). It is obvious that the $d_{x^2-y^2}$ gap rather than the horizontal line node gap better reproduces the experimental data. In particular, the absence of the dip of $A_4(\theta)$ at θ = 90 deg confirms the absence of a horizontal line node on the equator. These observations lead us to conclude that the superconducting gap in $CeIrIn_5$ is of $d_{x^2-y^2}$ type gap, as in $CeCoIn_5$ and $CeRhIn_5$. The establishment of the identical gap symmetry in CeMIn$_5$ (M = Co, Rh, and Ir) indicates the universality of the pairing mechanism in this family and provides important hints for resolving the mechanism of the novel superconductivity.

References
[1] K. An *et al.*, Phys. Rev. Lett. **104**, 037002 (2010).
[2] T. Park, E. D. Bauer, and J. D. Thompson, Phys. Rev. Lett. **101**, 177002 (2008).
[3] Y. Kasahara *et al.*, Phys. Rev. Lett. **100**, 207003 (2008).
[4] H. Shakeripour *et al.*, Phys. Rev. B **82**, 184531 (2010).
[5] S. Kittaka *et al.*, Phys. Rev. B **85**, 060505(R) (2012).

Authors
S. Kittaka, Y. Aoki, T. Sakakibara, A. Sakai, S. Nakatsuji, T. Tsutsumi[a], M. Ichioka[a], and K. Machida[a]
[a]Okayama University

A Proton-Electron Coupled Molecular Conductor: Charge-Order Driven Proton Arrangement

Mori Group

There has been much attention on proton dynamics in a hydrogen-bond (H-bond) in a wide range of scientific fields from chemistry and physics to biology and materials science [1].

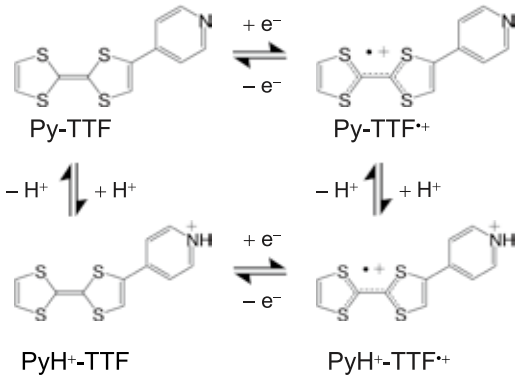

Fig. 1. A proton and an electron transfer process in Py–TTF.

For example, in the quinhydrone complex, the proton transfer through an intermolecular H-bond associated with the electron transfer between the π-electronic systems gives rise to a unique phase transition in the single crystal under high hydrostatic pressure. Recently, H-bonded supramolecules demonstrate to be organic ferroelectrics, where proton dynamics are deeply related to π-electron based molecular orbitals. However, proton-electron coupled phenomena in the H-bonded molecular conductors have been little explored to date.

In order to construct proton-electron coupled system in molecular conductors, we have focused on 4-pyridyl-substituted TTF derivative (PyTTF), where a strong electron donating TTF is directly bonded to a pyridyl substituent with both proton accepting (H-bonding) and electron withdrawing abilities (Figure 1). In this study, we have synthesized the proton-electron coupled CT complex based on PyTTF and an organic acceptor, tetrafluorotetracyanoquinodimetane (F_4TCNQ). The complex is formulated as $(PyH^+–TTF^{0.3+}Py–TTF^{0.7+})(F_4TCNQ^{\bullet-})_2$•MeCN (**1**), containing the dimer structure where PyTTFs are jointed by H-bond (Figure 2). Detailed X-ray analysis by using synchrotron radiation reveals that proton arrangement of **1** is determined by the charge pattern of donor molecules, and we termed this state as "charge-order driven proton arrangement." In this paper, we report the crystal structure and the electrical conductivity of **1**.

The synchrotron X-ray diffraction was employed to experimentally determine the crystal structure including the position of the protons. In the crystals, there are five crystallographically independent molecules: two donors, two acceptors and one acetonitrile molecule as a crystal solvent. The donor molecules are connected by N^+–H•••N type H-bond. The intra– and intermolecular distances N^+–H and N-N are 0.82(5) Å and 2.781(3) Å, respectively. In the IR spectrum of **1**, a broad peak was observed in 1800 – 2800 cm^{-1}. This corresponds to the NH stretching absorption of N^+–H•••N type H-bond.

In order to reveal the oxidation state of TTF moieties of donors A and B, we examined the charges for each molecule. In the IR spectrum, a lower wavenumber shift in the CN stretching mode was observed meaning that the charges of both acceptors C and D are –1. Since the net charges of the acceptors are –2, the net charge of donors A and B including the proton is estimated to be +2. The TTF moieties of the donors A and B are nearly planar and the dihedral angles between the TTF moiety and the pyridyl group of donors A and B are 15.14(6)° and 14.99(6)°, respectively. The central C=C bonds of the TTF moieties for donors A and B are 1.357(3) Å and 1.380(3) Å, respectively. These values are intermediate between neutral Py–TTF [1.344(9) Å] and cation radical salt of TTF [1.393 Å] indicating that donors A and B are partially oxidized. Each charge of TTF moieties of donors A and B was estimated to be +0.3 and +0.7 from their bond lengths. This estimation revealed that TTF moieties of donors A and B have different oxidation states and indicates the charge disproportionaion in the H-bonding unit. This charge disproportionation was also confirmed by the unrestricted density functional theory (DFT) calculation with the basis set 6-311G(d, p). These charge estimations provided the composition of **1** involving the charges of each molecules: $(PyH^+–TTF^{0.3+}Py–TTF^{0.7+})(F_4TCNQ^{\bullet-})_2$•MeCN.

To clarify the reason why the proton is located close to the donor A in the H-bond, the potential curve of proton was calculated by the unrestricted DFT calculation (Figure 3). It is known that an N^+–H•••N type H-bond exhibits a double –well potential curve of proton coordinates when an N–N distance is more than 2.5 Å. The calculated curve shows a double–well potential predicted from the N-N distance of **1** [2.781(3) Å]. The curve exhibits an asymmetric shape in which the charge disproportionation in H-bonding unit is reflected and takes a minimum energy level close to donor A containing charge-poor $TTF^{0.3+}$ moiety. This is due to suppress the intramolecular Coulomb repulsion between TTF moiety and pyridinium group. It is likely that this effect causes the proton ordering, suggesting a proton-electron coupled state in **1**.

Finally, we investigated the effect of the charge ordering on the conductivity. The complex exhibits semiconducting behavior with room temperature resistivity of 44 ohm cm and activation energy of 0.12 eV. The complexes with 1:1

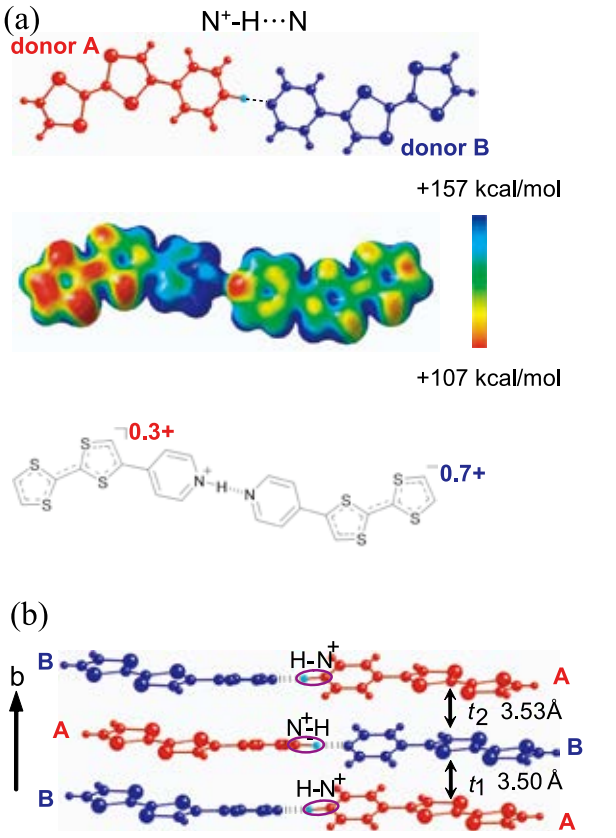

Fig. 2. (a) Structure of the H-bonded Py-TTF dimer by the X-ray crystal structure analysis and its electrostatic potential surface calculated by Gaussian 03 at the UB3LYP/6-311G(d,p) level of theory and (b) donor and proton arrangements in the CT complex along the b-axis, where the proton-electron coupled state as "charge-order driven proton arrangement" is realized.

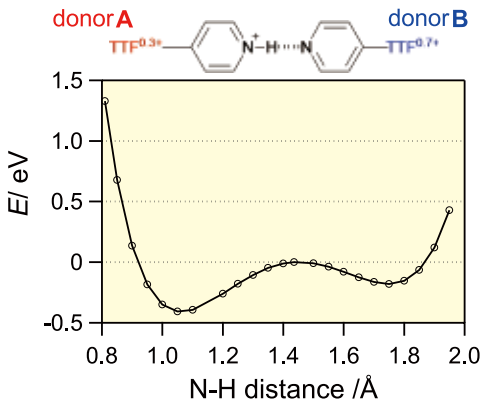

Fig. 3. N^+-H distance dependence of the energy potential difference ΔE of the H-bonded dimer calculated by the UB3LYP/6-31G(d) level of theory. The initial molecular geometry (N^+-H = 0.82 Å) was taken from the crystal structure, and the ΔE at 1.44 Å is set to 0 eV. The asymmetric shape where the minimum energy level (1.05 Å) is close to donor **A** with the charge-poor $TTF^{0.3+}$ moiety suggests that the Coulomb repulsion between the positive charges of the TTF moiety and the proton is much smaller at the charge-poor donor **A** side.

stoichiometry of donor to F_4TCNQ ratio have a tendency to show high resistivity around 10^4 ohm cm because the strong electron accepting ability of F_4TCNQ causes a fully–reduced state in CT salts. However, the complex **1** showed a resitivity less than typical 1:1 F_4TCNQ salts by two orders of magnitude. This indicates that the relatively high conductivity of **1** is originated from charge-ordered donor column. In addition, this results support the existence of proton because if proton didn't exist, fully-oxidized TTF would form a completely-filled band structure. Moreover, the resistivity is tremendously suppressed by pressure under 1.8 GPa by three orders of magnitude at room temperature, indicating the suppression of the charge ordering. The behaviors of protons coupled with melting of the charge ordering under pressure is the next research target.

In summary, we have successfully prepared the protonated CT complex based on pyridyl-substituted TTF derivative. The asymmetrical double-well proton potential in which the charge disproportionation is reflected explained the reason why a proton in H-bond is ordered. Proton arrangement in donor columns is determined by the pattern of charge ordering, and therefore we named this novel proton-electron coupled system as "charge-order driven proton arrangement". In this system, we believe that proton dynamics coupled with a change of electronic state by external stimuli such as electric field, light, pressure, etc. is observed.

References

[1] T. Mitani, G. Saito, and H. Urayama-Mori, Phys. Rev. Lett. **60**, 2299 (1988); H. Suzuki, H. Mori, J. Yamaura, M. Matsuda, H. Tajima, and T. Mochida, Chem. Lett. **36**, 402 (2007); H. Ohchi, K. Takahashi, J. Yamaura, S. Takaishi, and H. Mori, Physica B **405**, S341 (2010).

Authors

S. Lee, K. Takahashi[a], A. Ueda, T. Isono, A. Nakao[b], R. Kumai[c], Y. Murakami[c], and H. Mori

[a]Kobe University

[b]Research Center for Neutron Science and Technology, CROSS

[c]Condensed Matter Research Center, Institute of Materials Structure Science, KEK

Electrostatic Charge Carrier Injection into a Charge Ordered Organic Insulator

Tajima Group

Charge carrier injection into a strongly correlated insulating state often leads to drastic phenomena. Previously, charge carrier injection into such materials was achieved by chemical substitution. However, the structural inhomogeneity, which originates from the random arrangement of chemically substituted atoms, is not avoidable. In contrast to the conventional chemical method, electrostatic (ES) charge carrier injection using a field-effect-transistor (FET) structure has recently been focused. This method does not introduce structural inhomogeneity, and precise and repeatable control of the carrier concentration can be realized by varying the gate voltage.

Here, we report the ES charge carrier injection effect on an organic charge ordered (CO) material α-ET_2I_3 using a FET structure [1]. ET denotes BEDT-TTF = bis (ethylenedithiolo) tetrathiafulvalene. In the CO state, the strong electronic correlation plays an essential role as well as the Mott insulator. At ambient pressure, α-ET_2I_3 has a metal-insulator (MI) transition at 135 K, which is associated with charge ordering. Figure 1(a) shows the typical device structure that was measured in this study. The devices are prepared by laminating a thin single-crystal flake [typical dimensions of 100 mm x 50 mm x (thickness: $t \approx$ 200-600 nm)] on a highly-doped Si substrate with thermally-oxidized SiO_2 layer (500 nm). The SiO_2 layer and the highly-doped Si act as a gate insulator and a gate (G) electrode, respectively. The S and D electrodes are formed by Au evaporation in vacuum (thickness ~30 nm) through a metal mask. Figure 1(b) shows the temperature dependence of the S-D conductivity for each devices. The steep decease in the conductivity corresponds to the MI transition of α-ET_2I_3. Below 110 K, the conductivities approximately exhibit thermal activation behavior: $\alpha(T)$ is proportional to $\exp(-\Delta/k_BT)$ (Δ: activation energy, k_B: Boltzmann constant). The activation energies are approximately 550-650 K, depending on the devices.

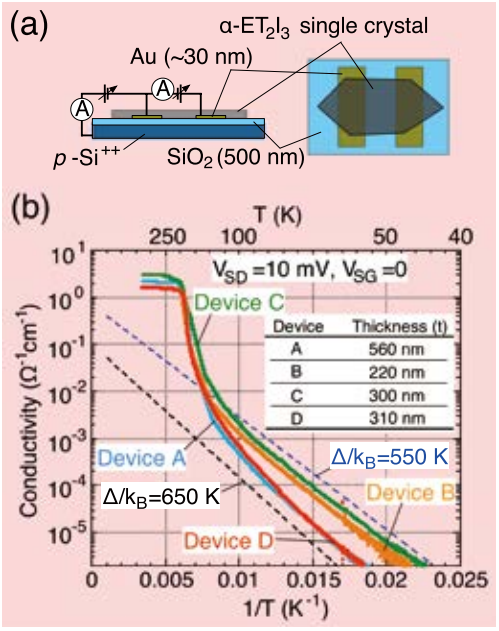

Fig. 1. (a) Schematics of typical FET device structure measured in this study. (b) Temperature dependence of S-D conductivity with zero gate voltage for four devices, A-D. Thickness (t) of α-ET2I3 crystals are summarized in the table (inset).

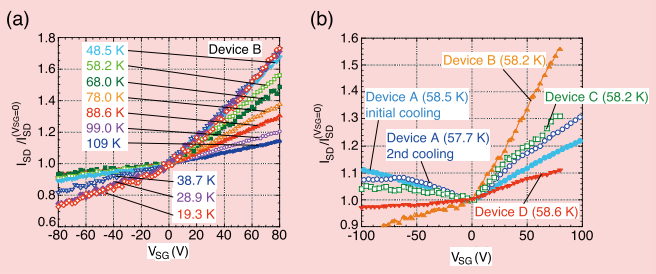

Fig. 2. (a)V_{SG} dependence of I_{SD} at various temperatures for device B. Data are normalized by I_{SD} for $V_{SG} = 0$ at each temperature. (b)Transfer characteristics of the four devices at approximately 58 K.

Figure 2(a) shows gate voltage dependence of normalized S-D current [$I_{SD}/I_{SD}(V_{SG} = 0)$] at various temperatures for device B. Below the MI transition temperature (T_{MI}), I_{SD} increases (decreases) for $V_{SG} > 0$ (< 0): *n*-type transfer characteristics are observed. In bulk crystals, the dominant carriers above T_{MI} are holes; however this changes to electrons below T_{MI}, so that *n*-type behavior would be reasonable. However, in the present study, we have observed bipolar characteristics in certain devices [see Fig. 2(b)], whereas only *n*-type behavior in the insulating state has previously been reported [2]. As can be seen in Fig. 2(b), the hole transport for V_{SG} strongly depends upon the device under investigation. Moreover, even in the same device, bipolar behavior, in particular that related to hole transport, is suppressed by the repetition of measurements and cooling-heating cycles. This means that the device dependence of hole transport is not sensitive to the device structure, but is, instead, dominated by the conditions of the (α-ET_2I_3)-Au and/or (α-ET_2I_3)-SiO_2 interfaces. These two interface conditions affect the contact resistance and the channel conductivity, respectively, and they determine the transport properties of the hole channel.

The electric field effect observed in our present study [$I_{SD}/I_{SD}(V_{SG}=0)$ ≈1.7 at the maximum] is rather small compared with the result of recently reported organic FET that uses a κ type ET Mott insulator [3]. The difference between these two devices may be interpreted as the presence or absence of a structural change in the two insulating states. In the case of α-ET_2I_3, the structural transition associated with charge ordering is observed, and stabilization of the CO state by the low-temperature structure has been suggested theoretically [4]. Therefore, the electronic phase transition is hard to occur, in contrast to in the Mott insulator, where lattice distortion at the MI transition is absent. Because the CO state has a non-uniform charge distribution (depending on each site), change in the crystal structure would be induced by the charge inhomogeneity. On the other hand, one electron is localized per site in the Mott insulating state, so that the charge distribution is homogeneous.

References
[1] M. Kimata, T. Ishihara, and H. Tajima, J. Phys. Soc. Jpn to be published.
[2] H. M. Yamamoto *et al*., Physica B: Condensed Matter **404**, 413 (2009).
[3] Y. Kawasugi *et al*., Phys. Rev. Lett. **103**, 116801 (2009).
[4] Y. Tanaka, and K. Yonemitsu: J. Phys. Soc. Jpn. **77**, 034708 (2008).

Authors
M. Kimata, T. Ishihara, and H. Tajima

Spin-Orbital Short-Range Order in the Honeycomb Based Lattice of $Ba_3CuSb_2O_9$

Nakatsuji Group

Nature favors the lowest energy so called ground state of a system, but at high temperatures disorder, called entropy, is dominant and provides the driving force for fascinating behavior such as phase transition from solid to liquid and from liquid to gas. Conversely, when temperature is lowered, the system solidifies because atoms or molecules, which move relatively freely in gas or liquid phase, spontaneously break the symmetry of the system to reduce its energy, leading to variety of intriguing phenomena. However, in some cases the liquid state can survive down to lowest temperature by lowering its quantum mechanical energy, which is known as quantum liquid. Examples are the superfluidity of Helium and the superconductivity of electrons. These quantum states have attracted much attention not only as a scientific subject of importance, but also as a subject in an applied research because of its robustness against disorder and the absence of dissipation at the quantum level.

Recent studies on magnets revealed that, under particular circumstances, the spins and orbitals which carry magnetism can remain liquid down to the lowest temperature with unbroken symmetry. This unusual behavior has attracted much attention because of its possibility as a new quantum liquid. It has been recognized, however, that such a liquid state of spin or orbital character is fragile and is easily frozen by, for example, structural disorder in magnets. In the present study on a copper oxide, we have discovered a new quantum liquid state that is robust against disorder by controlling cooperative phenomenon of spins and orbitals in electrons of copper atoms [1].

The material is $Ba_3CuSb_2O_9$, consisting of electric dipoles formed by a pair of divalent copper ions (Cu) and pentavalent antimony ions (Sb). This material was previously considered to be a ferroelectric in which the electric dipoles form a triangular lattice [2,3]. However, our recent diffraction measurements using synchrotron x-ray at SPring-8 revealed that the intrinsic aspect of this material is frustration on triangular lattice, and, as a result, the electric dipoles spontaneously form a short range ordering, which intrisically stabilizes the disordered honeycomb lattice of CuO_6 octahedra against the Jahn-Teller distortion.

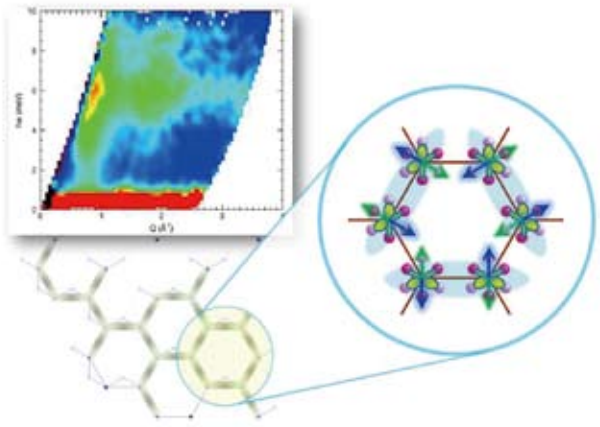

Fig. 1. Top left: Energy gap of spin liquid state revealed by inelastic neutron scattering experiments at 25 K. Bottom left: Short-ranged honeycomb-based lattice of $Ba_3CuSb_2O_9$ Right: Spin-orbital quantum state on the honeycomb-based lattice. Neighboring orbitals (green) forms a ferro-order. Arrows (blue and green) and blue shaded regions indicate spin-singlet dimers having a spin gap.

Generally, cations with orbital degrees of freedom exhibit orbital order by lowering the symmetry of the spatial distribution of surrounding anions (ligands) so that the electrostatic energy of each orbital is reduced. This phenomenon is called "Jahn-Teller phase transition". The typical example of this phenomena are copper oxide based materials famous for high-temperature superconductivity, and it is known that all copper oxide based materials have a Jahn-Teller phase transition.

In this work we have performed a comprehensive study of structural and magnetic properties of $Ba_3CuSb_2O_9$ using high-quality single crystal samples, and discovered that this material shows neither magnetic ordering nor a macroscopic Jahn-Teller phase transition down to low temperature. In addition, neutron scattering measurements (US-Japan Cooperative Program) revealed that copper ions form a dimer, a local resonant state of $S = 1/2$ of a copper ion and a neighboring copper ion (Fig. 1). On the other hand, X-ray absorption fine structure measurements found that all copper ion sites undergo Jahn-Teller distortion for short time scale as well as for local length scale. These observations indicate two possibilities: firstly, the orbitals order with a ring pattern along the honeycomb hexagon so that the spins can form the pair of the local spin dimer and secondly, both spins and orbitals cooperatively form a dynamic state which is a quantum mechanical resonant state (Fig. 1).

The realization of state without macroscopic Jahn-Teller phase transition in copper oxides is quite remarkable, and this state may stabilize a spin liquid, a novel quantum mechanical state. Furthermore, this state originates from a self-assembly of copper ions due to the electrostatic interaction between electric dipoles made by copper and antimony. This indicates that the quantum properties in condensed matter can be controlled using the pattern of electric dipoles, and provides an importance guide for future materials development. The present discovery of a material that shows quantum liquid state robust against disorder can open a new route to exploring materials required for the practical development of quantum information processing and quantum computing.

References

[1] S. Nakatsuji, K. Kuga, K. Kimura, R. Satake, N. Katayama, E. Nishibori, H. Sawa, R. Ishii, M. Hagiwara, F. Bridges, T. U. Ito, W. Higemoto, Y. Karaki, M. Halim, A. A. Nugroho, J. A. Rodriguez-Rivera, M. A. Green, and C. Broholm, Science **336**, 559 (2012).
[2] V. P. Köhl, Z. anorg. allg. Chem. **442**, 280 (1978).
[3] H. D. Zhou, E. S. Choi, G. Li1, L. Balicas, C. R. Wiebe, Y. Qiu, J. R. D. Copley, and J. S. Gardner, Phys. Rev. Lett. **106**, 147204 (2011).

Authors

S. Nakatsuji, K. Kuga, K. Kimura, R. Satake[a], N. Katayama[a], E. Nishibori[a], H. Sawa[a], R. Ishii[b], M. Hagiwara[b], F. Bridges[c], T. U. Ito[d], W. Higemoto[d], Y. Karaki[e], M. Halim[f], A. A. Nugroho[f], J. A. Rodriguez-Rivera[g,h], M. A. Green[g,h], and C. Broholm[g,i]

[a]Nagoya University
[b]Osaka University
[c]University of California, Santa Cruz, USA
[d]Japan Atomic Energy Agency
[e]University of the Ryukyus
[f]Institut Teknologi Bandung, Indonesia
[g]National Institute of Standards and Technology, USA
[h]University of Maryland, USA
[i]Johns Hopkins University, USA

Anisotropic Heavy-Fermi-Liquid Formation in Valence-Fluctuating α-$YbAlB_4$

Nakatsuji Group

4*f* -based heavy-fermion (HF) systems have attracted much attention with interesting phenomena such as unconventional superconductivity and non-Fermi-liquid (NFL) behavior found in the vicinity of quantum critical points. Our recent studies have found the first Yb- ($4f^{13}$) based HF superconductivity with the transition temperature T_c = 80 mK in the compound β-$YbAlB_4$ [1, 2]. Pronounced NFL behavior above T_c and its magnetic field dependence indicate that the system is a rare example of a pure metal that displays quantum criticality at ambient pressure and close to zero magnetic field [1]. Furthermore, the *T/B* scaling found in our recent high-precision magnetization measurements clarifies its unconventional zero-field quantum criticality without tuning [3], which cannot be explained by the standard theory based on spin-density-wave fluctuations. In contrast to the canonical quantum critical materials, hard x-ray photoemission spectroscopy (HXPES) measurements have revealed a strongly intermediate valence of $Yb^{+2.75}$ [4], providing an example of quantum criticality in a mixed-valence system. Whether the valence fluctuation is relevant for the mechanism of quantum criticality and superconductivity is an interesting open question.

Here, we measured the specific heat, magnetization, and resistivity of α-$YbAlB_4$ down to very low temperature [5]. This compound is the locally isostructural polymorph of β-$YbAlB_4$ with a different arrangement of distorted hexagons made of Yb atoms [space groups *Pbam*(α-$YbAlB_4$) and *Cmmm*(β-$YbAlB_4$), see Fig. 1]. According to the HXPES measurement [4], α-$YbAlB_4$ also has an intermediate valence of $Yb^{+2.73}$. The results indicate a Fermi-liquid (FL) ground state for α-$YbAlB_4$ in contrast to the unconventional quantum criticality observed in β-$YbAlB_4$. Interestingly, both systems exhibit Kondo lattice behavior with a small renormalized temperature scale of T^* ~ 8 K, although both of them have a large valence-fluctuation scale of ~200 K. Below T^*, α-$YbAlB_4$ forms a heavy-Fermi-liquid state with an electronic specific heat coefficient $\gamma \sim 130$ mJ/mol K^2 and a large Wilson ratio greater than 7, which indicates a ferromagnetic correlation between Yb moments. A Kadowaki-Woods ratio is found that is similar to those found in the normal Kondo lattice systems and considerably larger than mixed valence systems. Furthermore, the resistivity of α-$YbAlB_4$ exhibits one of the strongest anisotropies in heavy fermions (Fig. 2). The ratio between in plane and *c*-axis resistivity ρ_{ab} and ρ_c, ρ_{ab}/ρ_c, reaches 11 at low temperatures

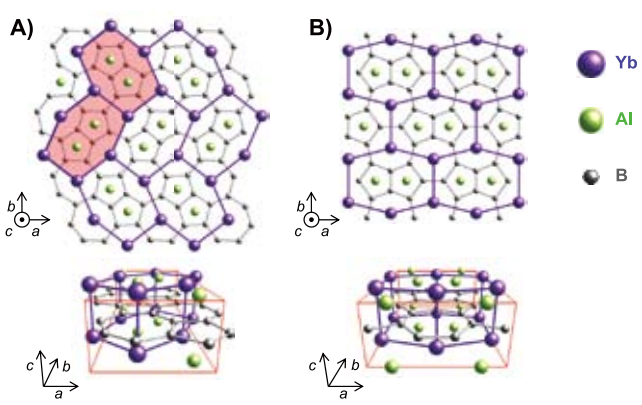

Fig. 1. Crystal structure of A) α-$YbAlB_4$ and B) β-$YbAlB_4$.

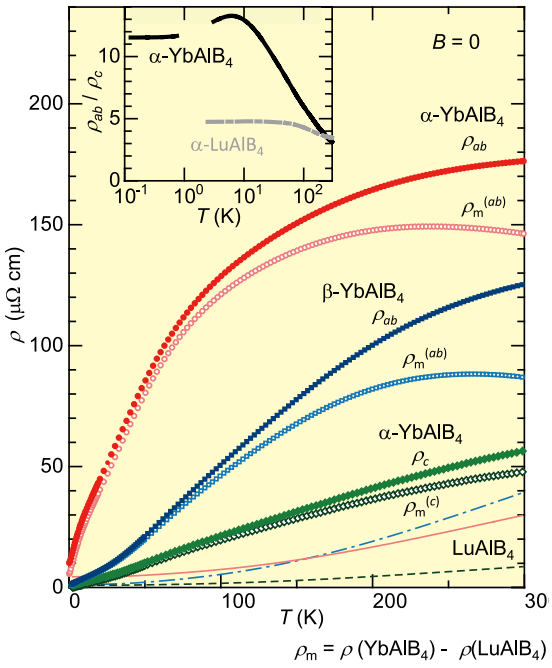

Fig. 2. Temperature dependence of the in-plane and c-axis resistivity ρ_{ab} and ρ_c of α-YbAlB$_4$ and ρ_{ab} of β-YbAlB$_4$. The magnetic part of the resistivity ρ_m is obtained by subtracting the nonmagnetic contribution estimated by ρ_{ab} of α- and β-LuAlB$_4$ (solid and dash-dotted lines, respectively) or ρ_c of α-LuAlB$_4$ (dashed line). The inset shows the temperature dependence of the ratios ρ_{ab}/ρ_c for α-YbAlB$_4$ and α-LuAlB$_4$.

below T^*. This strongly suggests anisotropic hybridization between 4f and conduction electrons which is stronger in the ab-plane. This is the key to understanding the mechanism of heavy-fermion formation as well as the Kondo lattice behavior found in the intermediate-valence system. Thus the system should be one of the best systems to study for elucidating the effects of anisotropic hybridization.

References

[1] S. Nakatsuji, K. Kuga, Y. Machida, T. Tayama, T. Sakakibara, Y. Karaki, H. Ishimoto, S. Yonezawa, Y. Maeno, E. Pearson, G. G. Lonzarich, L. Balicas, H. Lee, and Z. Fisk, Nature Physics **4**, 603 (2008).

[2] K. Kuga, Y. Karaki, Y. Matsumoto, Y. Machida, and S. Nakatsuji, Phys. Rev. Lett. **101**, 137004 (2008).

[3] Y. Matsumoto, S. Nakatsuji, K. Kuga, Y. Karaki, N. Horie, Y. Shimura, T. Sakakibara, A. H. Nevidomskyy, and P. Coleman, Science **331**, 316 (2011).

[4] M. Okawa, M. Matsunami, K. Ishizaka, R. Eguchi, M. Taguchi, A. Chainani, Y. Takata, M. Yabashi, K. Tamasaku, Y. Nishino, T. Ishikawa, K. Kuga, N. Horie, S. Nakatsuji, and S. Shin, Phys. Rev. Lett. **104**, 247201 (2010).

[5] Y. Matsumoto, K. Kuga, T. Tomita, Y. Karaki, and S. Nakatsuji, Phys. Rev. B **84**, 125126 (2011).

Authors

Y. Matsumoto, K. Kuga, T. Tomita, Y. Karaki[a], and S. Nakatsuji

[a]University of the Ryukyus

Kondo Effects and Multipolar Order in the Cubic PrTr_2Al$_{20}$ (Tr = Ti, V)

Nakatsuji Group

The Kondo effect, which screens magnetic dipole moments through the hybridization with conduction(c-) electrons, is known to provide a vast number of interesting phenomena such as heavy Fermions, quantum critical phenomena, and unconventional superconductivity. An interesting question is whether different type of Kondo effect is possible that screens orbital degree of freedom. Cox proposed such nonmagnetic version known as quadrupolar Kondo effect [1]. It was pointed out that quadrupolar Kondo effect arises if we consider orbital degree of freedom known as quadrupole moments of Γ_3 crystal electric field ground state in cubic $4f^2$ configuration. Interestingly, over-compensation by c-electrons may lead to anomalous metallic state far different from Fermi liquid [1]. Motivated by this proposal, several experimental studies have been done in Heusler-type compounds such as PrInAg$_2$ and PrMg$_3$ [2], [3] and nonmagnetic heavy fermion states are suggested due to the nonmagnetic Kondo effect. However, the Heusler-type compounds are known to have random site exchange that may lift the orbital degeneracy essential for the Kondo effect. On the other hand, if a system exhibits a quadrupole ordering, orbital degeneracy is assured above the ordering temperature. Therefore, it is ideal to study a system that allows tuning of quadrupole ordering temperature by changing the hybridization strength.

Here, we report the low temperature thermal and transport properties of PrTr_2Al$_{20}$ (Tr = Ti, V) by using high quality single crystals [4]. We revealed that PrTr_2Al$_{20}$ (Tr = Ti, V) is the first system that allows us to tune the hybridization strength and the quadrupolar ordering temperature: (i) A $-\ln T$ increase of resistivity ρ and large Weiss temperature θ_W of magnetic susceptibility χ indicate the Kondo effect, which is stronger in PrV$_2$Al$_{20}$ than PrTi$_2$Al$_{20}$. (ii) Quadrupolar ordering temperature T_Q = 2.0 K in PrTi$_2$Al$_{20}$ becomes lower to T_Q = 0.6 K in PrV$_2$Al$_{20}$. This hybridization difference can be attributed to (a) ~3 % unit-cell volume shrinkage by replacing Ti to V, and (b) additional 3d electron in V which should contribute to the conduction band. Moreover, anomalous metallic behaviors are observed in PrV$_2$Al$_{20}$ above T_Q such as $C_P/T \sim T^{-3/2}$, $\chi \sim T^{1/2}$, and $\rho \sim T^{1/2}$, most likely attributable to the quadrupolar Kondo effect. Further study is necessary to reveal how the quantum criticality appears by chemical substitution or applying pressure.

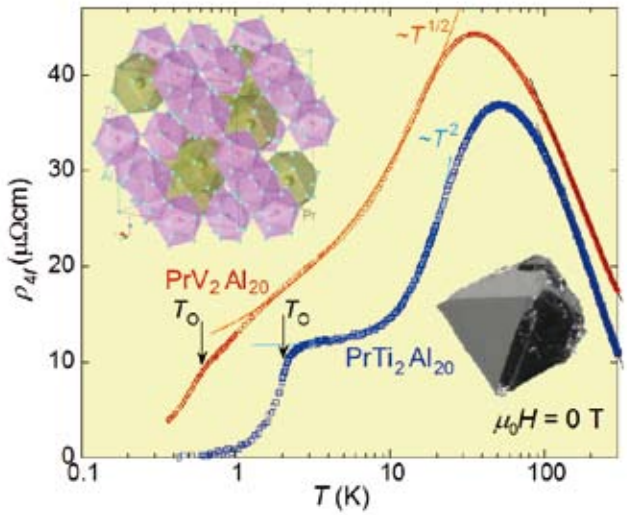

Fig. 1. Temperature dependence of 4f electron contribution to the resistivity. Arrows indicate the quadrupole order at T_Q = 2.0 K (PrTi$_2$Al$_{20}$) and 0.6 K (PrV$_2$Al$_{20}$). $-\ln T$ dependence of resistivity is observed above Δ ~ 60 K (PrTi$_2$Al$_{20}$) and ~ 40 K (PrV$_2$Al$_{20}$), indicating the magnetic Kondo effect. In contrast with Fermi liquid behavior with T^2 dependence (solid line) of the resistivity for PrTi$_2$Al$_{20}$, PrV$_2$Al$_{20}$ exhibits $T^{1/2}$ dependence (solid line) of the resistivity, suggesting the anomalous metallic state due to the quadrupolar Kondo effect. (Left inset) Crystal structure of PrTr_2Al$_{20}$. 16 Al ions around Pr lead to strong c-f hybridization. (Right inset) Picture of typical single crystal PrTi$_2$Al$_{20}$.

References
[1] D. L. Cox, Phys. Rev. Lett. **59**, 1240 (1987).
[2] A. Yatskar, W. P. Beyermann, R. Movshovich, and P. C. Canfield, Phys. Rev. Lett. **77**, 3637 (1996).
[3] H. Tanida, H. S. Suzuki, S. Takagi, H. Onodera, and K. Tanigaki, J. Phys. Soc. Jpn. **75**, 07370 (2006).
[4] A. Sakai and S. Nakatsuji, J. Phys. Soc. Jpn. **80**, 063701 (2011). Editor's Choice

Authors
A. Sakai and S. Nakatsuji

Hall Coefficient of Fe-based Superconductor $Ba_{1-x}K_xFe_2As_2$

Ohgushi Group

We have investigated the normal-state properties of the Fe-based superconductor $Ba_{1-x}K_xFe_2As_2$ by means of the Hall coefficient (R_H) measurements. R_H displayed in Fig. 1 exhibits a significant variation as a function of x and temperature (T). At $x = 0$, a negative R_H gradually increases in magnitude on cooling, shows a discontinuous jump at the Néel temperature, and reaches a constant value at 5 K. When holes are doped, R_H changes its sign. In a wide T range, R_H still shows a monotonic increase in magnitude on cooling; however, such a tendency becomes more moderate with increasing x. For $0.45 \leq x \leq 0.55$, we found a cross-over phenomena from the high-T increasing to the low- T decreasing behavior in R_H at $T \sim 100$ K, which is indicated by triangles in Fig. 1.

In order to interpret these complicated behaviors, we analyzed the data on the basis of the Boltzmann equation for a two-band system with a rigid-band approximation. We then got the following knowledge. (1) Holes with heavier mass at the Brillouin zone center feel less dissipation than electrons at the Brillouin zone corner. (2) Antiferromagnetic fluctuations, which can be monitored by a gradual increase of $| R_H |$ on cooling, gradually weaken with a departure from the antiferromagnetic phase in the x-T plane. (3) An anomalous coherent state characterized by heavy quasiparticles in hole bands evolves below $T \sim 100$ K, predominantly in the optimal and overdoped regions; this phase has a close connection with the pseudopeak observed in angle-resolved photoemission spectra [2].

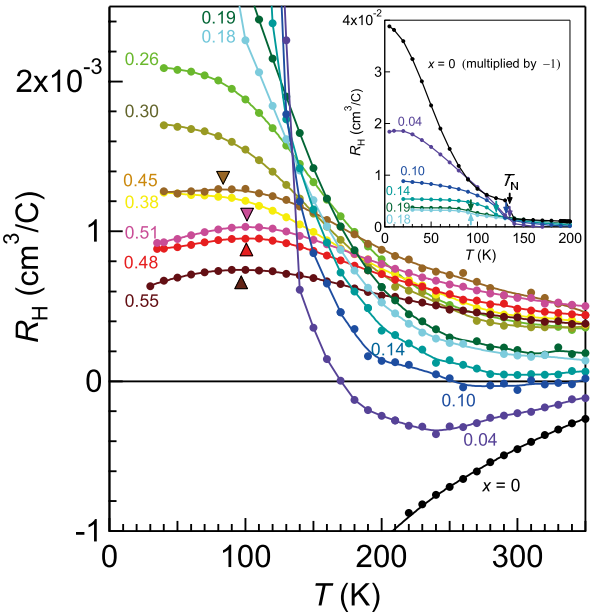

Fig. 1. Temperature (T) dependence of the Hall coefficient (R_H) for $Ba_{1-x}K_xFe_2As_2$ ($0 \leq x \leq 0.55$). The triangles indicate the crossover temperature, where R_H turns to a decrease on cooling. The inset shows R_H for samples which undergo the antiferromagnetic transition at low T in a full scale. The arrows indicate the antiferromagnetic transition temperature. Note that the data for $x = 0$ is multiplied by -1.

References
[1] K. Ohgushi, and Y. Kiuchi, Phys. Rev. B **85**, 064522 (2012).
[2] T. Shimojima, F. Sakaguchi, K. Ishizaka, Y. Ishida, T. Kiss, M. Okawa, T. Togashi, C.-T. Chen, S. Watanabe, M. Arita, K. Shimada, H. Namatame, M. Taniguchi, K. Ohgushi, S. Kasahara, T. Terashima, T. Shibauchi, Y. Matsuda, A. Chainani, and S. Shin, Science **332**, 564 (2011).

Authors
K. Ohgushi and Y. Kiuchi

Electric Dipolar Kondo Effect Emerging from Vibrating Magnetic Ion

K. Ueda Group

When a magnetic ion vibrates in a metal, it introduces a new channel of hybridization associated with phonon absorption or emission. When an ion is displaced it generally induces electric dipole moment. In such situation, we find that both the magnetic and electric dipole moments are quenched and that the ground state is characterized by spin singlet and parity singlet. In the simplest case of the s-wave localized orbital, the direct hybridization is with s-partial waves and the phonon assisted one with the p-partial waves. In this model, the total parity, which is defined by the number of phonons plus number of electrons in the p-channel by modulo two, is a good quantum number. The parity of the ground state is either even or odd. Just at the boundary between the two ground states with different parities, two-channel Kondo effect is generically observed [1, 2].

We find that the best quantity to discuss nature of the non-magnetic Kondo effect which is realized in the weak correlation regime is the susceptibility of the electric dipole moment [3]. When the electron phonon coupling is strong and at the same time the Coulomb interaction is weak, the

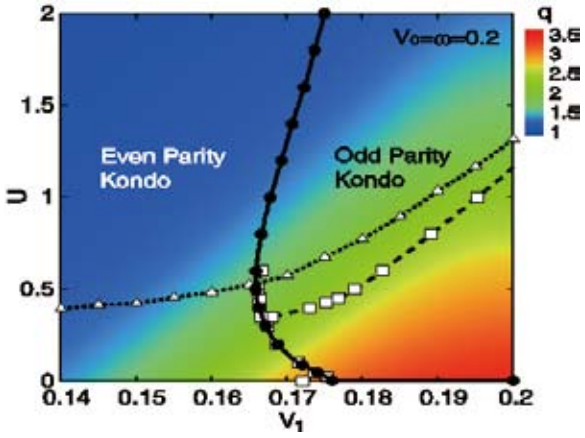

Fig. 1. Phase diagram in the parameter space of the phonon assisted hybridization with the p-wave conduction electrons, V1, and the Coulomb interaction, U [3]. In the blue region Kondo effect is characterized primarily by the screening of magnetic moment while in the red region by the screening of electric dipole moment. The ground state is spin-siglet and parity singlet with different parities, even on the left hand side but odd on the right hand side. At the boundary, two-channel Kondo effect takes place generically.

electric dipolar susceptibility shows a Curie law in a certain temperature range, which is a clear indication of the formation of electric dipole moment, doubly degenerate states with right polarization and left one. Below the Kondo temperature of the electric dipolar Kondo effect, the electric dipole moment starts to be quenched through the phonon assisted hybridization processes.

In the regime of the electric dipolar Kondo effect, electronic specific heat at low temperatures is generally enhanced. However, the enhancement factor is insensitive to magnetic field, except for the close vicinity of the line of two-channel Kondo fixed points.

References

[1] S. Yashiki, S. Kirino, and K. Ueda, J. Phys. Soc. Jpn. **79**, 093707 (2010).
[2] S. Yashiki, S. Kirino, K. Hattori, and K. Ueda, J. Phys. Soc. Jpn. **80**, 064702 (2011).
[3] T. Hotta and K. Ueda, arXiv:cond-mat/1203.4692, Phys. Rev. Lett. (to be published).

Authors

T. Hotta[a] and K. Ueda
[a]Tokyo Metropolitan University

Nonperturbative Conserving Approximation Scheme for Self-Consistent Calculation of the Electron Self-Energy

Takada Group

The electron self-energy Σ is a fundamental quantity in the Green's-function approach to the many-electron problem in solids. It is directly related to the one-electron spectral function $A(\boldsymbol{k},\omega)$ that can be observed experimentally by angle-resolved photoemission spectroscopy (ARPES). Accurate information on $\Sigma(\boldsymbol{k},\omega)$ in the wide range of momentum $\boldsymbol{k}$ and energy ω is useful not only for elucidating the detailed Fermi-liquid (FL) properties in usual metals but also for discussing the non-Fermi-liquid behavior inherent to the Tomonaga-Luttinger liquid (TLL) in systems with one spatial dimension.

Usually, Σ is calculated with use of many-body perturbation-theoretic (MBPT) methods, such as the Hedin's GW approximation (GWA). This GWA is a conserving approximation in the Baym-Kadanoff's sense, obeying the conservation laws of the *macroscopic* quantities like the *total* electron number, but because of the omission of all vertex corrections it does not satisfy the Ward identity (WI), an exact relation between Σ and the vertex function Γ due to gauge invariance representing the *local* electron-number conservation. Under the violation of the WI, an accurate enough Σ is not obtained in FL metals. In TLL metals, the situation becomes even worse, because any MBPT approach is inappropriate from the outset for describing the nonperturbative features of the TLL.

About a decade ago, a nonpertubative approach or the GWΓ scheme was developed for the self-consistent calculation of Σ[1], based on a rigorous algorithm to obtain the exact Σ as a fixed point of the self-energy revision operator [2]. This scheme always satisfies the WI and is applicable to both FL and TLL in a unified manner, but it encountered a serious problem in the electron liquid with the densities lower than the metallic ones; convergent results for Σ are not obtained, if its density specified by the dimensionless parameter r_s is larger than 5.25 at which there appears the dielectric catastrophe associated with the divergence of the compressibility κ and concomitantly that of the static polarization function Π in the long wave-length limit.

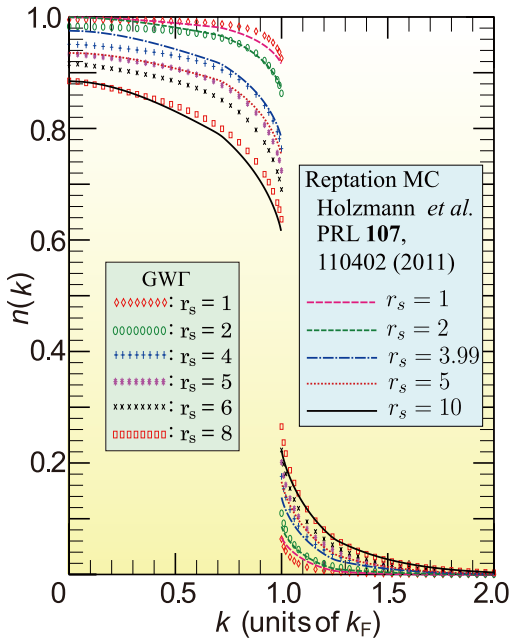

Fig. 1. Momentum distribution function $n(k)$ for the electron liquid at r_s=1 (diamond), 2 (ellipse), 4 (plus), 5 (star), 6 (cross), and 8 (rectangle) in the GWΓ method in comparison with those for r_s=1 (longer dashed), 2 (dashed), 3.99 (dotted-dashed), 5 (dotted), and 10 (solid) in the reptation Monte Carlo method.

In view of this situation, we have revised the original GWΓ scheme by (i) giving the better functional form for Γ based on a detailed analysis of the analytical structure of the exact Γ, (ii) modifying the scheme itself into the one free from the difficulty originating from the dielectric catastrophe, and (iii) proposing an alternative scheme on the condition that an accurate piece of information is available for Π by other calculations or experiments [3]. As an example to illustrate the power of our scheme, the results for the momentum distribution function $n(\boldsymbol{k})$ are shown in Fig. 1 in the low-density electron gas for r_s up to 8 in comparison with those recently obtained by the reptation Monte Carlo (RMC) method. In contrast to the inaccuracy in RMC, our results are so accurate that they all satisfy the important sum rules of $\Sigma_{k\sigma}k^{2n}n(k)$ for n=0 (total number), n=1 (kinetic energy), and even n=2 (fluctuation of kinetic energy) at least up to six digits.

In the future, we shall apply this scheme to real solids, along with (i) pursuing further analysis of the emergence of electron-hole asymmetric excitations, leading to a very characteristic $n(k)$ and a self-induced excitonic state for $r_s > 8$, and (ii) exhibiting transmutation from bosonic to fermionic natures with the increase of excitation energies in the one-dimensional TLL.

References

[1] Y. Takada, Phys. Rev. Lett. **87**, 226402 (2001).
[2] Y. Takada, Phys. Rev. B **52**, 12708 (1995).
[3] H. Maebashi and Y. Takada, Phys. Rev. B **84**, 245134 (2011).

Authors

H. Maebashi and Y. Takada

Dynamical Theory of Superfluidity in One Dimension

Oshikawa Group

Superfluidity is one of the most intriguing concepts in quantum physics, with a wide range of implications. On the other hand, importance of dimensionality has been recognized in many-body physics. While the physical space we live in is of three dimensions, construction of artificial structures with reduced dimensionality has made the effect of dimensionality relevant also in experimental studies. A fundamental question, which occurs naturally then, is the effect of dimensionality on superfluidity.

Superfluidity is often related to long-range ordering of quantum phase. The absence of the latter in two or lower dimensions at nonzero temperatures, which was proved mathematically, apparently implies there is no superfluidity in those dimensions. The experimental observation of superfluidity in two-dimensional ^{4}He film contradicts this argument. In fact, the superfluidity is more directly associated to non-vanishing helicity modulus, that is rigidity against phase twist. The helicity modulus does not vanish at sufficiently low temperatures even in two dimensions, despite the lack of the long-range order. This understanding of superfluidity in two dimensions was established in 1970s.

What about one dimension? In one dimension, the helicity modulus is known to vanish in the thermodynamic limit at any nonzero temperatures. This seems to imply the absence of superfluidity. Nevertheless, a recent torsional oscillator experiment [1] on ^{4}He confined in narrow one-dimensional channels revealed a superfluid response, calling for a new theoretical understanding.

We identify the superfluidity in one dimension as an essentially dynamical phenomenon, which is absent in strictly zero frequency limit. Peculiar nature of dynamics in one dimension however leads to an abnormally slow decay of current, which may be observed as superfluidity even at a very low frequency of torsional oscillators. Our theory reproduces main qualitative features of the experimental results, and predicts the frequency dependence of the "superfluid density" [2].

References

[1] J. Taniguchi, Y. Aoki, and M. Suzuki, Phys. Rev. B **82,** 104509 (2010); J. Taniguchi, R. Fujii, and M. Suzuki, Phys. Rev. B **84**, 134511 (2011).

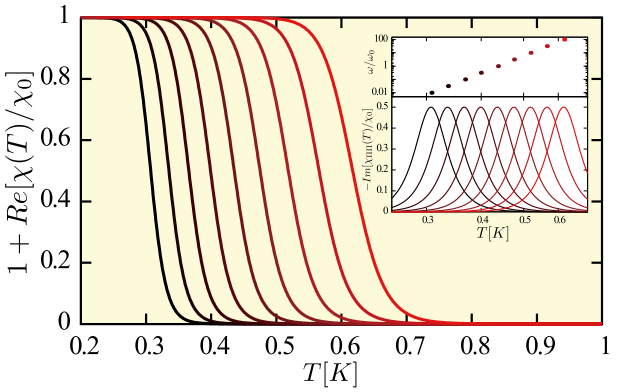

Fig. 1. (From Ref. [2]) Superfluid response for different probe frequencies, which ranges from $0.01\omega_0$ (dark) to $100\omega_0$ (bright), where ω_0 = 2kHz [1] and parameters are chosen to match the experiment. The inset shows the dissipation (lower part), and the frequency dependence of the peak temperature of the dissipation on a log-log scale (upper part). The frequency dependence shows the essentially dynamical nature of the superfluidity in one dimension.

[2] T. Eggel, M. A. Cazalilla, and M. Oshikawa, Phys. Rev. Lett. **107**, 275302 (2011).

Authors

T. Eggel, M. A. Cazalilla[a], and M. Oshikawa

[a]Spanish National Research Council and the University of the Basque Country

Magnetic Impurities in Spin Nematic State

Tsunetsugu Group

Quantum spin systems with strong frustration provide a nice playground for the quest of novel quantum orders. The spin-1 antiferromagnet with stacked triangular-lattice structure $NiGa_2S_4$ discovered by Nakatsuji Group has attracted attention of many experimental and theoretical groups to its spin-liquid like properties. Several theories have been proposed for their explanation, and one of the earliest is a spin nematic scenario put forward by our group. This can explain the absence of magnetic long-range order, particularly neutron scattering data, and power-law temperature dependence of specific heat at low temperatures, at least in qualitative level. However, this theory seems inconsistent with the divergent behavior observed by Ishida group in NMR relaxation rate around T^*~8.5K, which is usually attributed to some magnetic phase transition.

We have tried to explain this magnetic "instability" within the spin nematic scenario. One useful hint is μSR experiment performed by MacLaughlin and his colleagues. They reported the presence of slow spin dynamics even below T^* and its time scale is order of μs. Magnetic susceptibility also indicates a glassy behavior below T^*, but its glassy signal is very weak. Another hint is an unconventional impurity effect. Upon doping impurities, the freezing temperature T^* decreases, and this is opposite to the conventional case of canonical spin glasses where the freezing temperature is enhanced.

Our idea is that impurity magnetic moments establish unconventional type of interactions among them in the host with spin nematic order and that these interactions lead to a glass state of impurity moments with slow dynamics. The first program is to elucidate the nature of impurity interactions. This question is also interesting in that impurities may be used as useful probe to investigate host properties. A well-known example is RKKY interaction of magnetic impurities in metal, and it has two characteristics. One is a

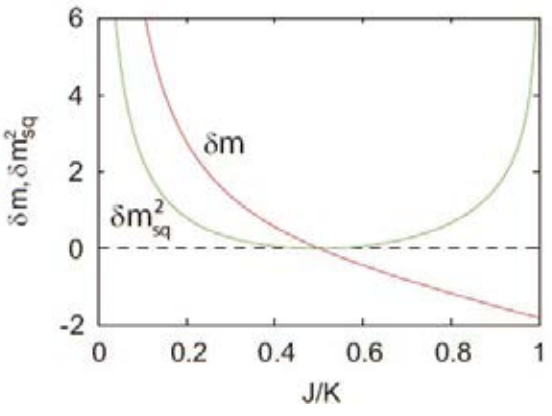

Fig. 1. Induced magnetic moments around impurity. δm is the total magnetization of induced moments, and δm_{sq}^2 is the sum of squared moments.

long-range nature; interaction decays in a power-law rather than exponential. The other is oscillation in space, and interaction changes from antiferromagnetic to ferromagnetic and vice versa with impurity distance. The first is a manifestation of the presence of zero-energy magnetic excitations in the host metal. The second is the consequence of the presence of a typical length scale, which is the inverse of the linear size of Fermi volume.

Our system has a characteristic that the host has a noncoplanar spin nematic order with a finite ordering wave vector. The spin nematic order has gapless nonmagnetic excitations as its Goldstone mode due to its spontaneous breaking of spin rotation symmetry. We have performed calculations in the sprit of RKKY interaction. We first calculate how a single magnetic impurity creates both nonmagnetic and magnetic excitations in its neighboring part of the host. To determine interaction between a pair of impurities, we then calculate the energy cost or gain due to overlap of these excitations created around each of the two impurities. The model is a spin-1 Hamiltonian with bilinear (J) and biquadratic (K) interactions of Ni-ion spins. This is a phenomenological model for investigating an antiferro spin nematic order, and the both J and K are antiferromagnetic. We have employed site-dependent mean-field approximation combined with analysis with effective field theory.

Solution of a single impurity problem provides two important results. The first point is that the host nematic order generates effective spin anisotropy of impurity moments. Details of anisotropy depend on the value of K/J, but in most of the parameter space considered ($0.087<J/K<1$), magnetic moments tend to move apart as much as possible from directors of the antiferro nematic order. In a narrow region near the boundary with the ferromagnetic phase ($0< J/K <0.082$), the easy axes are parallel to the directors instead. The second point is that there appear induced magnetic moments in a neighboring part of the host around the impurity. Figure 1 shows the total induced moment, and it is divergently enhanced near the border to ferromagnetic phase ($J/K \to 0$) or antiferromagnetic phase ($J/K \to 1$). This means that even when the impurity concentration is small, many magnetic moments are activated there. We have also calculated created nonmagnetic and magnetic excitations around the impurity. The results show that nonmagnetic one has a long tail in its spatial distribution, and this decay is proportional to 1/(distance). It also changes sign when one goes around the impurity site. Magnetic excitation is exponentially localized around the impurity, but its size is again divergently enhanced near the two borders, $\xi \propto (K/|K-2J|-1)^{-1/2}$.

We have calculated impurity-impurity interactions mediated by nonmagnetic and magnetic excitations around impurities. The dominant part is the contribution of nonmagnetic excitations, and its dependence on impurity-impurity distance is plotted in Figure 2. Decomposing it to its angular harmonics, we find that the L=2 mode is the largest component. This interaction changes its sign four times when one impurity moves around the other, and it has two important features. One is the long-range nature, i.e. dependence $\sim 1/r^2$. The other is that this is an interaction of spin quadrupole moments rather than dipole moments: the impurity Hamiltonian is biquadratic in their magnetizations. Since the interactions are long-ranged and oscillating in space, they stabilize a glassy state. However, this state differs in nature from the ordinary spin glass state in that the frozen degrees of freedom are spin quadrupoles rather than dipoles. Conventional pair-wise spin flips do not cost this energy, and they persist in the glassy phase. We expect that this is the origin of slow spin dynamics observed in μSR measurements. Since this long-range interaction is mediated by low-energy excitations in the ordered host, the glassy state should disappear together, when the spin nematic order vanishes. Thus, the freezing temperature T^* is determined by the bulk energy scale, and is suppressed by impurity doping. To provide quantitative predictions for the glassy state, we need further investigations, and we believe that this may be a good starting point.

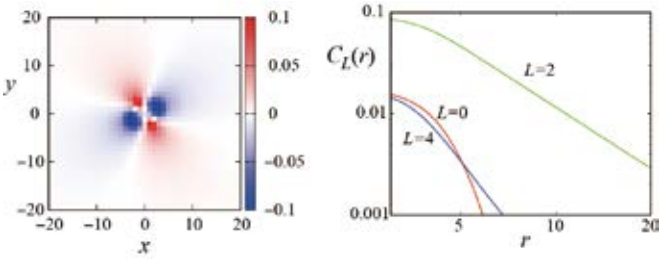

Fig. 2. Interactions between impurity moments mediated by nonmagnetic excitations in the host for J/K=0.5. Coordinates are measured in units of lattice constant, while the unit of interactions is K. (Right) Angular part decomposition of the interaction, $\Sigma_L C_L(r)\cos L\varphi$.

Reference

[1] J. Takano and H. Tsunetsugu, J. Phys. Soc. Jpn. **80**, 094707 (2011).

Author

H. Tsunetsugu

Full Counting Statistics for SU(N) Impurity Anderson Model

Kato Group

The distribution of current flowing through nanoscale-objects such as quantum dots has useful information on how electrons are transmitted. For example, the current noise (the second moment of the current distribution) calculated for the SU(2) Kondo dot revealed that the non-equilibrium backscattering current is composed of two types of electron transfer due to single quasiparticles and pairs of quasiparticles, carrying charge e and $2e$, respectively[1]. In other words, in addition to usual 'one-by-one' electron transfer, 'synchronized' transfer by paired electrons may occur due to strong Coulomb repulsions. The same result was obtained in a clearer way by direct calculation of the current distribution function in general formalism of the full counting statistics (FCS)[2].

In the present work[3], we extend the FCS approach to multiorbital Kondo dots, which can be experimentally realized in vertical dots, carbon nanotube, and double dots. We consider an SU(N) impurity Anderson model (see the inset of Figure1(a)) as a prototype model for examining multiorbital effects. This model assumes N-degenerate quantum states (including spin degrees of freedom) at an impurity site: the Kondo dots with one orbital and two degenerate orbitals corresponds to N=2 and 4, respectively. We theoretically find that current correlation through different orbitals provides a wealth of information if the system is in the non-equilibrium Kondo regime.

We calculate the Fano factor (the ratio between noise and backscattering current) for an SU(N) Anderson model,

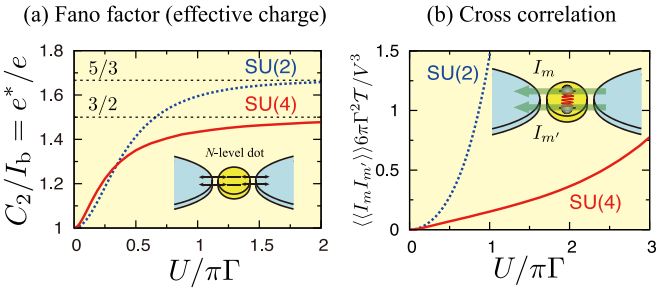

Fig. 1. (a) A Fano factor defined as a ratio between current noise and backscattering current, which is recognized as an average charge of transfer carriers. Inset: A schematic figure of an SU(N) Anderson impurity model. (b) Cross correlation between currents through different levels.

which can be recognized as an effective charge of carriers transmitting through a dot. The result for N=2 and 4 is shown in Fig. 1 (a). As the Coulomb repulsion increases, the Fano factor changes from 1 to 5/3 for N=2, and to 3/2 for N=4. This result suggests that 'synchronized' quasiparticle transfer with two electrons starts to work under strong Coulomb repulsions. The 'synchronized' quasiparticle transfer can be observed also in the current cross-correlation shown in Fig. 1 (b), where correlation between currents through different orbitals is induced by the Coulomb repulsion. As the number of degenerate orbitals increases, proportion of 'synchronized' quasiparticle transfer observed in the Fano factor is reduced, but remains a sufficiently large value for N=4. We note that cross correlation in the SU(4) case can be measured experimentally without any spin-dependent current detection, whereas cross correlation in the SU(2) case can also be measured in double-dot systems if a spin degree of freedom is replaced by a pseudo-spin assigned to electron configuration.

In summary, we have examined current correlation in an SU(N) Anderson model, and have shown that electron correlation between different orbitals, recognized as an 'orbital-singlet', produces current correlations for different orbitals, giving a direct measure of this synchronized transfer. Our calculation indicates that precise description of this effect needs careful consideration based on a non-equilibrium version of the local Fermi liquid theory. We expect that our result will be examined through current cross-correlation measurement in orbital-degenerate nanoscale objects.

References
[1] E. Sela, Y. Oreg, F. von Oppen, and J. Koch, Phys. Rev. Lett. **97**, 086601 (2006).
[2] A. O. Gogolin and K. Komnik, Phys. Rev. Lett. **97**, 016602 (2006).
[3] R. Sakano, A. Oguri, T. Kato, and S. Tarucha, Phys. Rev. B **83**, 241301(R) (2011).

Authors
R. Sakano, A. Oguri[a], T. Kato, and S. Tarucha[b]
[a]Osaka City University
[b]University of Tokyo

Fermi Surface Deformation near Charge-Ordering Transition

Kato Group

The shape of a Fermi surface (FS) is an important factor in determining the electronic properties of a metal. For many organic conductors, band structures are obtained by the extended Hückel method, and give an important starting point to understand material properties. The shape of the FS is probed with high sensitivity in transport measurements such as angle-dependent magnetoresistance oscillations, the Shubnikov-de Haas effect and magnetoresistance.

The shape of the FS may be modified by strong electronic exchange-correlation effects, which are neglected in band calculations. Deformation of the FS has been discussed on the basis of a single-band Hubbard model in the context of research of high-T_c superconductors. In several theoretical works, the FS was shown to be deformed so that its nesting condition improves at the wavenumber of the antiferromagnetic(AF) ordering. However, the degree of deformation obtained was small in these studies.

In this work, we study how the FS is deformed when the system approaches the charge-ordering(CO) transition, which is frequently observed in organic conductors. Starting with the extended Hubbard model on a square lattice and employing a fluctuation exchange (FLEX) approximation, we calculate one-particle Green's function near the CO transition. The calculated spectral functions $A(k, \omega{=}0)$ are shown in Fig. 1 (a), (b), and (c). In the present calculation, electron hopping, on-site Coulomb interaction, and temperature are fixed as t=1, U=5, and k_BT=0.1, respectively. We further change nearest-neighbor interaction V and second-nearest-neighbor interaction V' along one of the two diagonal directions by assuming V=V'. As V(=V') increases, charge fluctuations develope at the wave-number $\boldsymbol{Q}$=(2π/3, 2π, 3), and finally become divergent at V=2.52, indicating phase transition into a charge-modulated phase with a wavenumber $\boldsymbol{Q}$. As clearly seen in Fig. 1 (a)-(c), charge fluctuations develope near the CO transition change the FS shapes. Near the CO transition (see Fig. 1 (c)), the FS is deformed so that the wavenumber vector $\boldsymbol{Q}$ spans it well. We note that the FS is deformed in the Hartree-Fock(HF) approximation through hopping renormalization by off-diagonal Fock terms. However, the appearance of a flat part in the FS is not obtained in the HF approximation, since such a feature appears only when charge fluctuations are fed back into one-particle Green's function as done in the FLEX approximation.

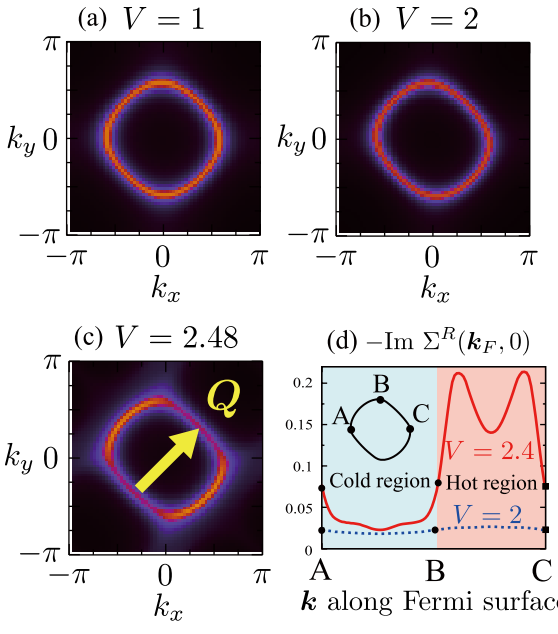

Fig. 1. Spectral functions $A(k, \omega{=}0)$ for (a) V=1, (b) V=2, and V=2.48. Red circles indicate the Fermi surfaces. Charge-ordering transition takes place at V=2.52. (d) Scattering rates (the imaginary part of the self-energy) on the Fermi surface. Lifetimes of quasiparticles become short(long) in the hot(cold) region.

As a result of the FS deformation, the quasiparticle-scattering anisotropy strengthens because the anisotropic self-energy is enhanced near CO. In Fig. 1 (d), we show the quasiparticle scattering rate $-\mathrm{Im}\Sigma^{R}(k, \omega=0)$ as a function of position on the FS. The inset of Fig. 1 (d) shows three FS points: the $-k_x$ direction (A), $+k_y$ direction (B) and $+k_x$ direction (C). The results show that the scattering rate is largely enhanced in the *hot* region BC (the flat part of the FS) as the system approaches the CO transition, whereas it remains small in the *cold* region AB. Formation of hot and cold regions reflects anisotropy in the exchange-correlation interaction potential, which becomes strong near the CO transition. This anisotropic quasi-particle scattering can be detected via the in-plane anisotropy of electronic, thermal conductivities, and magnetoresistances.

In summary, we have demonstrated that in contrast to AF spin fluctuations, the FS is largely modified near the CO transition. We emphasize that this remarkable change in FS originates from the large discrepancy between the CO wave vector and the nesting vector in a noninteracting system. As a result of FS deformation, quasiparticle properties become more anisotropic near the CO transition. We note that when the system is close to the CO transition, the FS is sensitive to changes in temperature and/or pressure because strength of charge fluctuations changes rapidly.

References

[1] H. Seo, J. Merino, H. Yoshioka, and M. Ogata, J. Phys. Soc. Jpn. **75**, 051009 (2006).

[2] K. Yoshimi, T. Kato, and H. Maebashi, J. Phys. Soc. Jpn. **80**, 123707 (2011).

Authors

K. Yoshimi[a,b], T. Kato, and H. Maebashi

[a]University of Tokyo

[b]Nanosystem Research Institute "RICS", AIST

Geometric Resonances in Hexagonal Lateral Superlattices – An Initial Step towards Artificial Graphene

Iye Group

A hexagonal lateral superlattice (LSL) – a two-dimensional electron gas (2DEG) subjected to periodic potential modulation having hexagonal-lattice symmetry – is of interest in two different directions. First, it is envisaged as a route to artificially generate massless Dirac fermions at the corners of the superlattice Brillouin zone [1]. Second, it is expected to stabilize the fragile "bubble phase" in the quantum Hall system (clusters of two or three electrons arranged in the hexagonal lattice, theoretically predicted to be the ground state at the 1/4 or 3/4 filling of the third or higher Landau levels [2]). As an initial step towards experimental verification of these fascinating possibilities, we study magnetotransport of hexagonal LSLs. We find three types of oscillations that evidence the hexagonal-lattice potential imposed on the 2DEGs [3].

The LSL devices are fabricated from conventional GaAs/AlGaAs 2DEGs. Periodic potential modulation is introduced via strain-induced piezoelectric effect by placing a hexagonal array of electron-beam (EB) resist pillars, with the lattice constant a = 100 nm or 200 nm, on the surface of the wafer (Fig. 1, left inset). The main panel of Fig. 1 shows

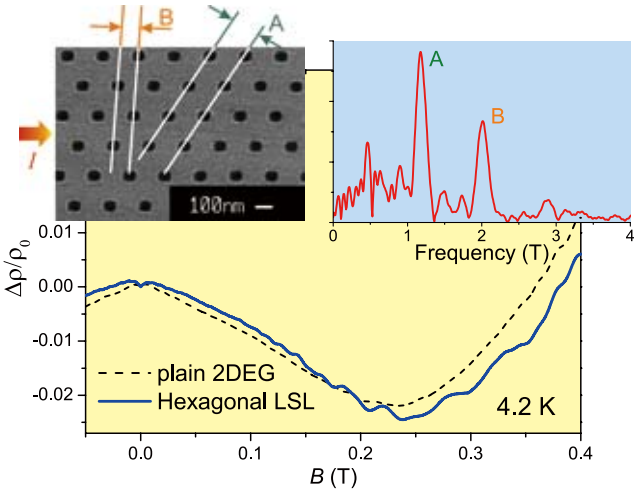

Fig. 1. Magnetoresistance $\Delta\rho/\rho_0$ of the hexagonal LSL (a = 200 nm) showing commensurability oscillations resulting from the periodicities A and B. Magnetoresistance of the plain 2DEG is also shown for reference. Left inset: Scanning electron micrograph of the hexagonal array of the EB resist (black dots). Periodicities A and B are indicated. Right inset: Fourier spectrum of the oscillatory part $(d^2/dB^2)(\Delta\rho/\rho_0)$ vs. $1/B$.

magnetoresistance traces of a hexagonal LSL with a = 200 nm at 4.2 K. Oscillations are observed above ~ 0.1 T. Fourier analysis shown in the right inset reveals that the oscillations are composed of two $1/B$-periodic components, attributable to the commensurability between the periodicity A (173 nm) and B (100 nm), respectively, depicted in the left inset, and the cyclotron radius R_c. At lower temperatures (~ 15 mK), Shubnikov-de Hass (SdH) oscillations are clearly resolved. In hexagonal LSLs, SdH oscillations exhibit amplitude modulation analogous to those observed in unidirectional LSLs [4]. The modulation can be explained by the commensurability oscillations of the Landau bandwidth due to the periodicity A, with the amplitude maxima taking place at the flatband conditions.

Closer inspection of lower magnetic field regime (B < ~ 0.1 T) divulges yet another type of oscillations having very small amplitudes, as displayed in Fig. 2 (c). A series of small peaks are ascribed to the occurrence of the geometric resonance of open orbits [5] composed of the segments of cyclotron orbits repeatedly diffracted by Bragg reflections

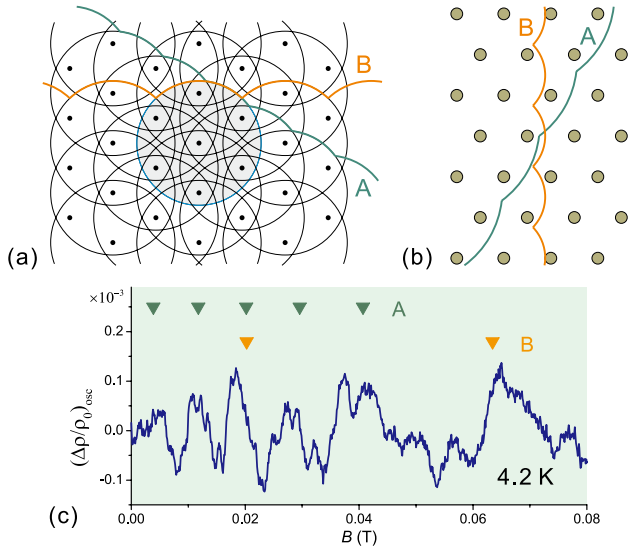

Fig. 2. (a) Hexagonal lattice in the reciprocal space, showing Fermi circles and open orbits originating from Bragg reflections due to periodicities A and B. (b) Open orbits in the real space. (c) Oscillatory part of the low-field magnetoresistance (obtained by subtracting slowly-varying background) of the hexagonal LSL (a = 200 nm). Downward triangles mark the magnetic fields for the geometric resonances of the open orbits A and B to take place.

(see Fig. 2 (a) and (b)). The width of the open orbits varies as $1/B$, and the resonance takes place at the magnetic field where the width coincides with the corresponding periodicity. The observation of these resonances demonstrates that the miniband structure brought about by the externally imposed hexagonal superlattice can be explored by the measurement of the magnetoresistance, and allows us to envision the possibility of observing the Dirac points by further decreasing the lattice constant and/or increasing the Fermi wavelength.

References

[1] C-H. Park and S. G. Louie, Nano Lett. **9**, 1793 (2009).
[2] A. A. Koulakov, M. M. Fogler, and B. I. Shklovskii, Phys. Rev. Lett. **76**, 499 (1996).
[3] Y. Kato, A. Endo, S. Katsumoto, and Y. Iye, Proc. 19th Int. Conf. on Electronic Properties of Two-Dimensional Systems (2011).
[4] A. Endo and Y. Iye, J. Phys. Soc. Jpn. **77**, 054709 (2008).
[5] A. Endo and Y. Iye, Phys. Rev. B **71**, 081303(R) (2005).

Authors

Y. Kato, A. Endo, and Y. Iye

Spin-Filtering and Detection in a Non-Magnetic Semiconductor Quantum Structure

Katsumoto Group

A key technology in semiconductor spintronics is the creation of spin-current. Especially the creation without the aid of ferromagnetism is a most important issue if one aims at the manipulation of quantum information associated with electron spins because ferromagnetism can be a strong source of quantum decoherence. In order to create spin polarization in a non-magnetic material, some mechanism to break the time-reversal symmetry is required. The combination of a current flow through a quantum point contact (QPC) and the spin-orbit interaction can work as such a device. The former works as a source of time-reversal symmetry breaking and the latter as a transducer to the spin-degree of freedom. The detection of spin polarization is also a problem to be solved. We have confirmed that a QPC in a material with a strong spin-orbit interaction can really work as a spin polarizer and a quantum dot (QD) can work as a sensitive detector.

A two-dimensional electron gas (2DEG) in an $In_{0.1}Ga_{0.9}As$ film was epitaxially grown on a GaAs substrate. The spin-orbit interaction in InGaAs is known to be much stronger than that in GaAs. A QD, which is composed of

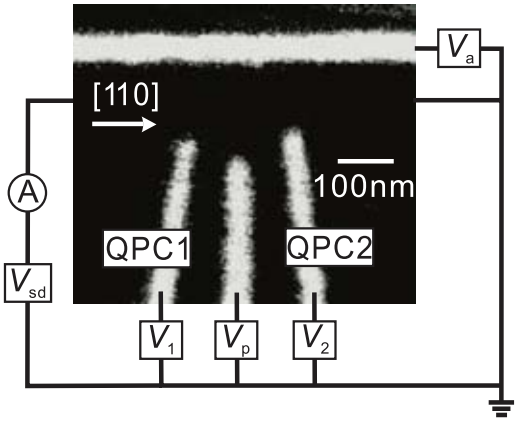

Fig. 1. Scanning electron micrograph of the gate configuration for the quantum dot defined in a 2DEG of an $In_{0.1}Ga_{0.9}As$. White regions indicate the Schottky gates made of Au-Ni.

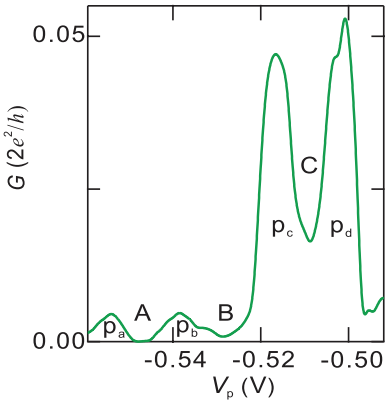

Fig. 2. Four successive Coulomb conductance peaks of the QD. Apparently they are classified into two pairs, which is the result of the Kramers degeneracy. The pair with higher conductance is showing conductance enhancement in the valley region due to the Kondo effect.

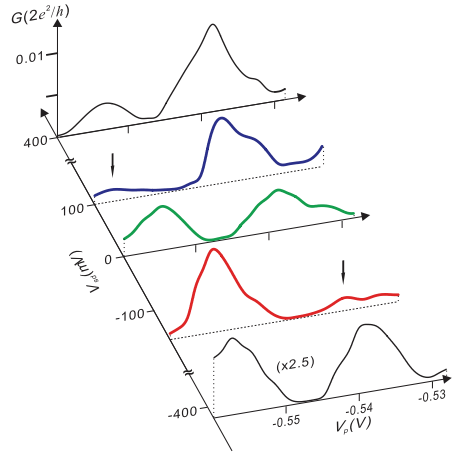

Fig. 3. Anti-symmetric disappearance of the Coulomb peaks with the application of the source-drain voltage to the QD (Red and blue curves. Indicated by vertical arrows).

two QPCs and a center plunger gate was defined with metal Schottky gates. The gate configuration is shown in Fig.1. The conductance through each QPC was quantized with the unit of e^2/h, which is half of the usual quantization unit. This "half-quantization" is a sign of spontaneous spin-polarization.

In order for the confirmation with a more spin-specific phenomenon, the Coulomb oscillation in the QD was measured. In Fig.2, we observe two pairs of the Coulomb conductance peaks, one of which is much higher than the other. This is due to the appearance of the Kondo effect, which manifests at the same time that the Coulomb valley (the intermediate region between the two peaks) has a spin 1/2 or an odd number of electrons.

Now knowing the spin states in the Coulomb valleys, we turn our attention to the other pair of conductance peaks. As shown in Fig.3, one of the peaks diminished with applying a source-drain voltage (V_{sd}) to the QD while the other peak diminished with a source-drain voltage with the opposite sign. The twin-peak structure was recovered with further increase of the voltage. This anomalous behavior of the Coulomb peaks on the source-drain voltage can be explained in detail with assuming that the spin filtering effect. In other words, the anti-symmetric disappearance of the Coulomb peaks evidences the spin-filtering effect through a QPC with the spin-orbit interaction.

Reference

[1] S. W. Kim, Y. Hashimoto, Y. Iye, and S. Katsumoto, J. Phys. Soc. Jpn. **81**, 063004 (2012).

Authors

S. W. Kim, Y. Hashimoto, and S. Katsumoto

Dynamics of Coupled Vortices in a Pair of Ferromagnetic Disks

Otani Group

Magnetic vortex is one of the fundamental spin structures in submicron-sized ferromagnetic elements. It is characterized by two degrees of freedom, i.e., the in-plane curling magnetization "chirality (c = ±1)" and the out-of-plane magnetization "polarity (p = ±1)". In the low frequency excitation state, called the "gyration mode", the vortex core with perpendicular magnetization rotates around its equilibrium position. This is analogous to a motion of point mass in a harmonic potential. When magnetic vortices are arranged at a distance of submicron, they are coupled through dipolar interaction induced by the surface magnetic charges on the edges. Especially a pair of magnetic vortices can be regarded as an "artificial" molecule bound via the dipolar interaction. As in the case of a diatomic molecule with the van der Waals bonding, the energy levels of the artificial molecule (bonding and anti-bonding states) should depend on the combination of chiralities and polarities. Furthermore, by arranging the magnetic vortices in a two-dimensional array, one could expect the so-called "magnonic crystal" [1]. In spite of such a high potentiality for application, there are few experimental reports on the coupled vortices via direct exchange interaction and also dipolar interaction in physically separated vortices. In this work, we demonstrate the experimental evidence of the resonant excitation of a magnetostatically coupled pair of vortices as a clear mode splitting of spectra.

Figure 1 (a) shows our experimental setup. To detect the gyration mode, we adopted the spin torque diode effect via the anisotropic magnetoresistance of permalloy (Py) disks. When an *ac* current is injected into a Py disk, the vortex core gyrates only at the resonant frequency. In this process, the magnetoresistance of the Py disk also oscillates with the same frequency. As a result, a *dc* voltage is generated only at the resonant frequency. As shown in Fig. 1(b), a clear resonant mode is detected at 220 MHz. This resonant frequency is reproduced by our micromagnetic simulation (see the top panel of Fig. 1(d)).

When two Py disks are arranged in a pair with a separation distance of ~100 nm (see Fig. 1(a)), a coupled vortex core motion should be reflected on the *dc* voltage. As can be seen in Figs. 1(b) and 1(c), a single resonance line observed for the single disk splits into two resonance lines and there appear in total four different modes depending on the product of two polarities p_1p_2 [2]. Compared with our micromagnetic simulations, the observed four different modes can be identified with the polarities p_1p_2, chiralities c_1c_2 of the two vortex cores (see Fig. 1(d)). The unique property in this system gives us a guiding principle for designing the magnonic crystal in further expanded systems such as one-dimensional chains and two-dimensional arrays and is a candidate for novel tunable oscillators using vortices.

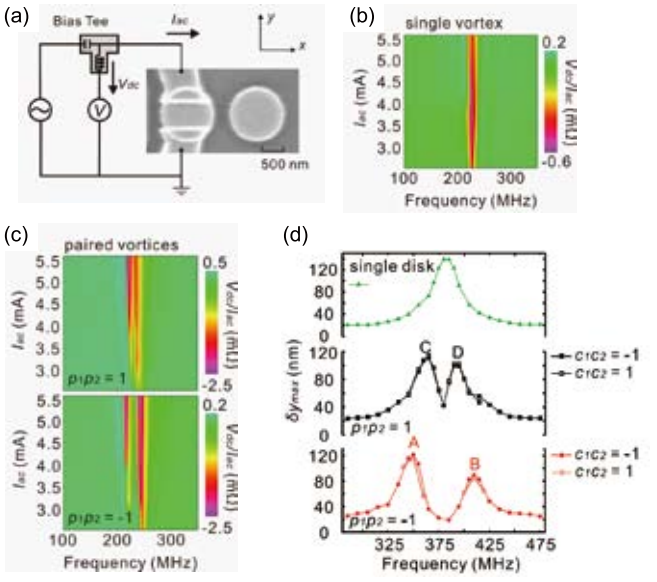

Fig. 1. (a) Schematic diagram of our measurement setup for the spin torque diode effect and a scanning electron microscopy image of the sample. (b), (c) Frequency and power dependencies of the normalized *dc* voltage V_{dc}/I_{ac} measured for an isolated disk (b) and for the paired disks with different polarities (c). (d) Simulated core displacement for a single vortex as well as for a pair of vortices. As mentioned in the main text, such a core displacement results in a *dc* voltage via the spin torque diode effect.

References

[1] J. Shibata and Y. Otani, Phys. Rev. B **70**, 012404 (2004).
[2] S. Sugimoto, Y. Fukuma, S. Kasai, T. Kimura, A. Barman, and Y. Otani, Phys. Rev. Lett. **106**, 197203 (2011).

Authors

S. Sugimoto, Y. Niimi, Y. Fukuma[a], S. Kasai[b], A. Barman[c], and Y. Otani
[a]Kyushu Institute of Technology
[b]National institute for Material Science
[c]S. N. Bose National Center for Basic Science

One-dimensional Fermi Surface for an Anisotropic Two-dimensional Metallic State at Au-adsorbed Ge(001) Surface

Komori Group

Electronic structure of the Au-adsorbed Ge(001) surface with a one-dimensional (1D) atomic structure has been studied as one of the low dimensional metallic states. A

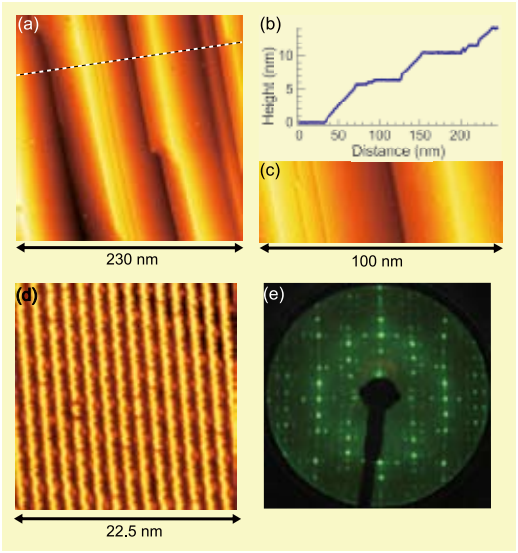

Fig. 1. (a) STM image of a Au-adsorbed vicinal Ge(001) surface, which consists of (001) areas with Au-induced chains and step-bunched areas. Gold was deposited on the clean substrate of 4 degree off to the [110] direction at 740 K, (b) Cross section along the dotted white line in (a). A step-and-terrace structure is evident. (c) Magnified STM image of a part of the surface shown in (a). Gold-induced chains parallel to the step edges are seen on the (001) surface. No periodic structure was observed on the step-bunched areas. (d) Atomic image of the chain structure on the (001) terrace. The sample bias voltage was −1 V. Eight-fold periodicity in the chain direction is clearly shown as the presence of the dots in the groove between the chains. (e) Typical LEED pattern of the single-domain surface at 60 eV.

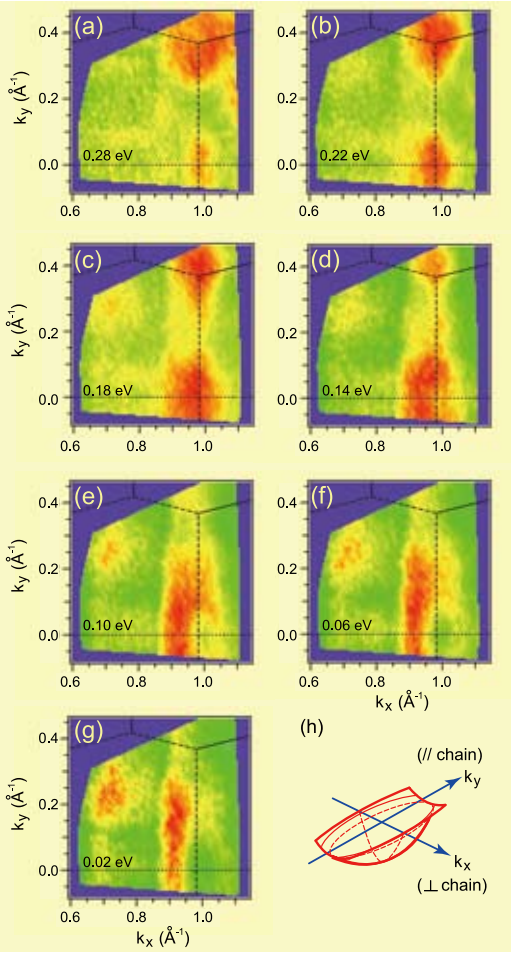

Fig. 2. (a-g) Constant-energy ARPES intensity maps of the metallic band around (k_x, k_y) = (0.98 Å^{-1}, 0 Å^{-1}) for the binding energy = 0.28 (a), 0.22 (b), 0.18 (c), 0.14 (d), 0.10 (e), 0.06 (f) and 0.02 eV (g). The chain direction is parallel to k_y. The ARPES intensity is plotted after normalization of each spectrum by its total intensity. The width of the energy window is 20 meV. Intensity is the highest in the red area, and the lowest in the green area. Dispersion in the chain direction is smaller than that in the direction perpendicular to the chain. (h) Schematic model of the metallic band.

1D metallic state was claimed on the basis of the results of scanning tunneling spectroscopy and Fermi surface mapping [1] while the metallic state shows anisotropic two-dimensional dispersion in the study of angle-resolved photoemission spectroscopy (ARPES) [2]. The exact position of the band bottom in the surface Brillouin zone (SBZ) and the direction of the strong dispersion have not been fixed because the surfaces with two domains on a flat Ge(001) substrate were used in all the previous experimental studies. We have studied the electronic states by ARPES using single-domain samples on a substrate tiled to the [110] direction to understand this interesting low-dimensional system.

Figure 1 shows the results of scanning tunneling microscopy (STM) and low energy electron diffraction. They indicate the formation of the single-domain surface with the well-known atomic chain structure that is commonly observed on the flat substrates [3]. The surface consists of the chains parallel to the step edges. The separation of the adjacent chains is 1.6 nm, and an 8-fold periodicity can be seen in the chain direction. The symmetry of the surface structure has been considered to be c(8x2) while some of the observed LEED spots do not belong to this symmetry. [2]

Constant-energy ARPES intensity maps of the metallic band for a single-domain surface are shown in Figs. 2(a-g). The band bottom of the metallic state is found at the zone boundary ($\bar{J}$ point) of the c(8x2) SBZ as in Figs. 2(a-d). The band shows dispersion in the both parallel and perpendicular directions to the chain. (Fig. 2(d-f)) Contrary to our intuitive expectation, direction of the strong band dispersion is perpendicular to the chain. At the energy close to E_F, the band is almost parallel to the chain as in Fig. 2(g) just like a 1D electronic state in the direction perpendicular to the chain. A schematic model of the metallic band is shown in Fig. 2(h). This state has a very unique band shape.

References
[1] S. Meyer *et.al*. Phys. Rev. B **83**,121411(R) (2011).
[2] K. Nakatsuji *et. al.*, Phys. Rev. B **80**, 081406 (2009).
[3] R. Niikura *et. al.*, Phys. Rev. B **83**, 035311 (2011).

Authors
K. Nakatsuji, Y. Motomura, R. Nikura, and F. Komori

Two-dimensional Superstructures of Cyclohexane on Rh(111) : Effects of Preadsorbed Hydrogen

Yoshinobu Group

Adsorption of alkane molecules on metal surfaces is an important subject in various fields. In particular, activation of C-H bonds of adsorbed alkanes through interaction with metal surfaces is a key process of dehydrogenation on heterogeneous catalysts. In order to understand the reaction mechanism, it is essential to elucidate the adsorption states and the nature of the adsorbate-metal interaction. Most of the

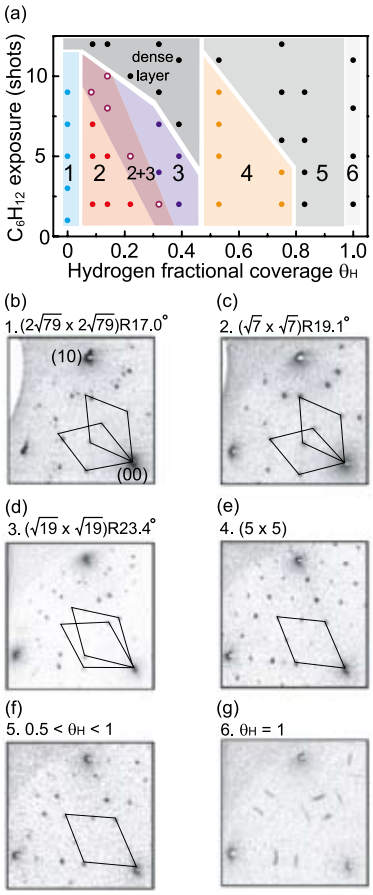

Fig. 1 (a) A phase diagram of superstructures observed by SPA-LEED as a function of cyclohexane exposure and coadsorbed hydrogen coverage. All measurements were carried out at 90 K, and data points are indicated by dots. (b) – (g) SPA-LEED patterns of overlayer structures 1 to 6 in (a), together with the notations of the commensurate and HOC structures. The incident electron energy is 75 eV. Reciprocal unit cells of cyclohexane domains are indicated by lines.

previous studies deal with the adsorption of alkanes on clean metal surfaces. There are few studies concerning adsorption on hydrogen-preadsorbed metal surfaces, although it is a more relevant system for elucidating the reaction mechanism of the hydrocarbon conversion reaction which is usually performed in excess hydrogen.

In this study, we investigated adsorption structures and interaction of cyclohexane molecules on the clean and hydrogen-preadsorbed Rh(111) surfaces using scanning tunneling microscopy (STM), spot-profile-analysis low-energy electron diffraction (SPA-LEED), temperature-programmed desorption (TPD), and infrared reflection absorption spectroscopy (IRAS) [1]. Various ordered structures of adsorbed cyclohexane were observed as a function of hydrogen and cyclohexane coverages. When the fractional coverage (θ_H) of preadsorbed hydrogen was below 0.8, four different commensurate or higher-order commensurate superstructures were found as a function of θ_H; whereas more densely packed incommensurate overlayers became dominant at higher θ_H (Fig. 1). IRAS measurements showed sharp softened C-H vibrational peaks at 20 K, which originated from the electronic interaction between adsorbed cyclohexane and the Rh surface. The multiple softened C-H stretching peaks in each phase are due to the variation in the adsorption distance from the substrate. At high hydrogen coverages they became attenuated in intensity and eventually diminished at $\theta_H = 1$. The gradual disappearance of the soft mode correlates well with the structural phase transition from commensurate structures to incommensurate structures with increasing hydrogen coverage. The superstructure of adsorbed cyclohexane is controlled by the delicate balance between adsorbate-adsorbate and adsorbate-substrate interactions which are affected by preadsorbed hydrogen.

Reference
[1] T. Koitaya, K. Mukai, S. Yoshimoto, and J. Yoshinobu, J. Chem. Phys. **135**, 234704 (2011).

Authors
T. Koitaya, K. Mukai, S. Yoshimoto, and J. Yoshinobu

Clustering and Merging of Vortices in Nano-Size Superconductors

Hasegawa Group

Nano-size superconductors exhibit unique properties which are different from macroscopic counterparts since the characteristic size is in the same order of the coherence length. Here we demonstrate one of them; clustered and merged vortices on Pd nano island structures observed in real space by using low-temperature scanning tunneling microscopy (STM).

When magnetic field is applied on type-II superconductors, vortices or quantized magnetic fluxes are formed. Because of the Meissner current circulating around them, these entities repel each other, and thus stabilized by forming of the triangular Abrikosov lattice. In the case of the nano-size island superconductors, the mutual interaction among the vortices is modified by the lateral confinement, and unique states or configurations which are not found in macroscopic superconductors, such as giant vortex and anti-vortex, are created.

The vortices in the Pb nano-size superconductors can be visualized by using low-temperature STM with a capability of magnetic field application. Since the superconductivity is locally broken at the core of the vortices, the position of the vortices can be directly imaged by measuring the superconducting gap at the every site by the tunneling spectroscopy. Using a 3He-cooled ultrahigh vacuum (UHV) STM setup with a superconducting magnet we have demonstrated various phenomena on the nano-size superconductors, *e.g.* island-size dependence of the vortex penetration field and the existence of the minimum critical size for the vortex formation, by making images showing vortex distribution of various sizes of islands as a function of the applied magnetic field.

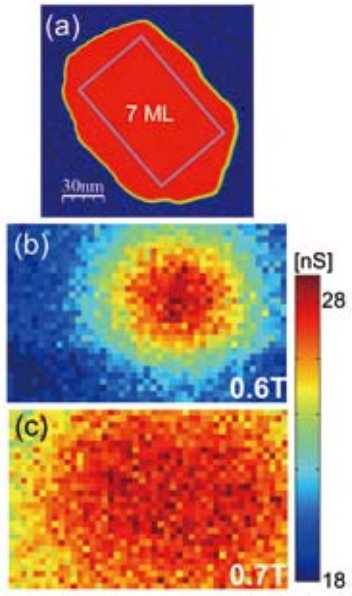

Fig. 1. (a) STM image of a Pb island structure whose thickness is 7 monolayer (2.0 nm). (b, c) mappings of the tunneling conductance at zero bias voltage taken at 0.6 T (b) and 0.7 T (c). Reddish color, indicating high tunneling conductance, shows superconductivity-broken area and corresponds to vortex (vortices).

Figure 1(a) shows an STM image of a Pb island. The island was prepared on a Si(111) substrate by depositing Pb in the UHV condition. Because of the *in situ* preparation, the sample is atomically flat-topped with a (111) surface and clean without any contaminations or oxide layers. From the STM image, the size, shape and thickness of the island can be measured exactly in atomic scale precision. The coherence length of 7 monolayer (ML) Pb thin film is 34 nm. Under the magnetic field, we measured tunneling spectra and

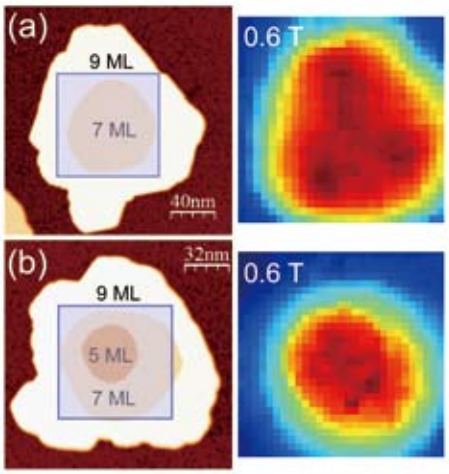

Fig. 2. STM image (left) and the zero-bias-voltage tunneling conductance image taken in the square area under 0.6 T (right) on two islands having a void structure.

mapped out the tunneling conductance at zero bias voltage, that is, at the bottom of the superconducting gap. The conductance images shown in Fig. 1(b, c) are taken in the rectangular area shown in the STM image (a) at the magnetic field of 0.6 T and 0.7 T, respectively. In these images vortices are observed as a reddish (high conductance) region around the center of the island. While the island has a circular high conductance region, which obviously corresponds to a single vortex, at 0.6 T (b), the high conductance region of 0.7 T (c) is elongated; different from the one found at 0.6 T in shape. We believe the elongated one is due to two vortices merged into a single one, that is, a giant vortex with a vorticity of 2.

Similar state of vortices was also observed on Pb islands having a void structure. Because of the thinner thickness and the smaller condensation energy, the voids trap vortices. Figure 2 shows two sets of an STM image and a conductance map taken on islands with a void structure. In the conductance map of (a), three vortices are trapped in the void, forming a cluster. On an island having a deeper void (Fig. 2(b)), where the trapping energy is larger, three vortices are further squeezed to form a single giant vortex around which the phase variation of the macroscopic wave function is 3 times 2π.

These unique vortex states have been a subject of extensive studies both experimentally and theoretically. Unique capability of STM; visualizing the shape of the vortex states and configurations and directly linking them to local structures of the superconductors, will provide a significant contribution to solve the relevant issues.

References

[1] T. Nishio *et al.*, Phys. Rev. Lett. **101**, 167001 (2008).

[2] T. Tominaga *et al.*, J. Supercond. Nov. Magn. (2012), DOI 10.1007/s10948-012-1522-4.

Authors

T. Tominaga, T. Sakamoto, T. Nishio, T. An, T. Eguchi, Y. Yoshida, and Y. Hasegawa

Ferroelectricity in Magnetite

Lippmaa Group

Magnetite Fe_3O_4 is among the oldest known naturally-occurring magnetic materials. The ferrimagnetic order in magnetite is derived from unequal numbers of spins in two antiparallel Fe sublattices divided among the tetrahedral and octahedral sites of the spinel crystal structure. Magnetite is metallic at room temperature, but a charge-ordered

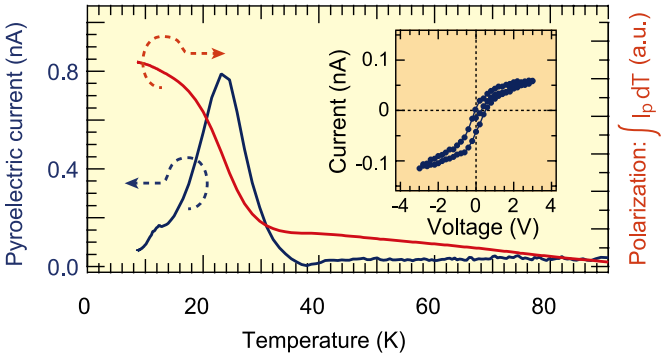

Fig. 1. Temperature dependence of the measured pyroelectric current amplitude under periodic heating of a thin film Fe_3O_4 sample capacitor. The measured current can be integrated to obtain a polarization curve. By also applying periodic poling bias pulses, the ferroelectric polarization loop can be measured (inset).

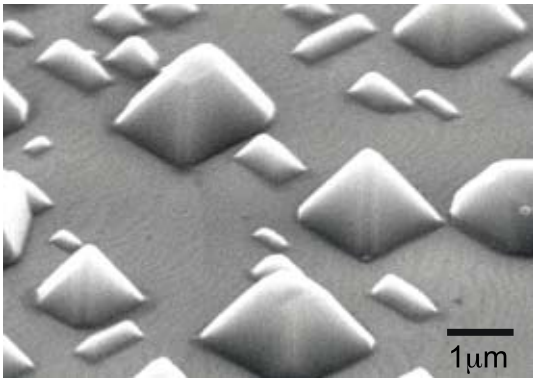

Fig. 2. Scanning electron microscope image of nanoscale magnetite pyramids with a (001) lattice orientation grown by a self-template technique on a (001) $SrTiO_3$ substrate.

state appears when a crystal is cooled below the Verwey temperature of about 125 K, resulting in a sharp increase of resistivity. The charge-ordered state has been predicted to be polar and ferroelectric, but accurate measurement of ferroelectric polarization is difficult due to the relatively low resistivity of magnetite just below the Verwey transition temperature.

A number of zero-bias techniques can be used to accurately measure the ferroelectric polarization, even in materials that are not insulators. We have chosen to use a pyroelectric technique, where a miniature thin-film capacitor is periodically heated with a focused laser beam. Since the polarization of ferroelectrics is temperature dependent, it is possible to measure the derivative of the polarization-temperature curve by integrating the current flowing in or out of the sample capacitor during periodic heating and cooling. Since no bias is applied to the capacitor during measurement, characterization for ferroelectric polarization is not affected by leak currents. Figure 1 shows an example of a pyroelectric polarization measurement for a thin magnetite film. Integrating the pyroelectric current is used to obtain the polarization curve, while a ferroelectric hysteresis curve is obtained by poling the ferroelectric capacitor with short applied bias pulses and varying the applied pulse amplitude between -3 and +3 Volts. It is clear that the magnetite film shows spontaneous polarization below about 40 K and the polarization direction can be switched by applied bias.

Ferroelectricity in oxides is usually related to the freezing of a soft mode that results in a structural phase transition. Magnetite is an interesting case, since Raman spectroscopy measurements show no structural transitions in magnetite films below the Verwey temperature. The appearance of ferroelectricity can therefore be assumed to be caused by a purely electronic mechanism, related to bond dimerization in the charge-ordered state. In order to further study the ferroelectric transition in magnetite, it is important to obtain films with a well-defined crystal orientation and to avoid the appearance of a random multidomain state. We have developed a self-template thin film growth technique for fabricating such films on (001)-oriented $SrTiO_3$ single-crystal substrates. The technique is based on higher-order lattice matching that allows the much larger Fe_3O_4 spinel lattice to form an epitaxial film on a perovskite $SrTiO_3$ substrate. The higher-order lattice-matched magnetite buffer layer must be grown at low temperatures to stabilize the thermodynamically unfavorable (001) film surface. Once the buffer has been grown, a thick magnetite film can be grown at high temperature without losing the desired (001) lattice orientation. Very high-quality films can be grown even at 1100 °C, where surface faceting leads to the formation of nanoscale

pyramids (Fig. 2), while still maintaining the (001) lattice orientation. We expect such nanopyramids to be good candidates for obtaining small single-domain magnetite crystallites for pyroelectric characterization of the ferroelectric state in Fe_3O_4.

Reference
[1] R. Takahashi, H. Misumi, and M. Lippmaa, Cryst. Growth and Design **12**, 2679 (2012).

Authors
R. Takahashi, H. Misumi, and M. Lippmaa

Vortex State in hcp solid ^{4}He

Kubota Group

Superfluidity has been found not only in the liquid state of two isotopes of He, but also in electrons (superconductivity) in solids as well as in dilute gas systems. As to much higher density systems, possible superfluidity in the solid state had been discussed since early days from 1956 by Penrose and Onsagar with negative result [1]. Positive theoretical discussions for the superfluidity in solids were strengthened in 1960's and quite positive expectations were expressed by various groups in the world in 1969 and 1970[2]. Since then a lot of experimental efforts to find it out took place over the world including Japanese groups. It is, however, 2004 when the first convincing evidence was presented as a possible observation of the non-classical rotational inertia (NCLI) in solid He[3]. 8 years have passed since then yet the real happening in the solid He is still controversial [4].

The Kubota group had been developing a technique to study essential features of superfluids in an superfluid made of 3D connected He monolayer superfluid film[5] using a technique combining highly sensitive torsional oscillator (TO) detection and DC rotation of the sample (whole cryostat) at very low temperatures. TO measures the moment of inertia, through which change of momentum of the bob where the sample is located is detected. For a superfluid non-classical rotational inertia *NCRI* is measured as a decrease of the moment of inertia. More generally the decrease of the moment of inertia is expected for a vortex fluid state and the TO response is called nonlinear rotational susceptibility *NLRS* after Anderson [6]. TO measures also the Q value change through which the energy dissipation in the system is measured. DC rotation of the superfluid sample would cause vortex lines through the superfluid/supersolid. They [5,7,9] discovered a new way of detecting quantized vortex lines through the sample utilizing the fact that the circulating superflow around each of the vortex lines penetrating through the sample interacts with quasi particles in the system and causes extra energy dissipation [5]. Highly sensitive torsional oscillator technique has been employed for the study of solid He as well under DC rotation [7] to detect the extra dissipation below a transition temperature T_c, below which macroscopic coherence is expected to be established in the system. Evidence for the vortex lines penetration was found. In addition they found the occurrence of the hysteretic behavior just below the same T_c and argued that one branch of the hysteretic loop expels the vortices from the sample and the difference between the two branches of the NLRS gives the supersolid density ρ_{ss}. Rather complicated situation in the study of the vortex state and the supersolid state in hcp ^{4}He is clarified in the recent review paper by Minoru Kubota[8] from the independent different kinds of quantitative measurements on the same samples. Namely the supersolid density ρ_{ss} is derived from the hysteretic component of the NLRS and the energy dissipation caused by introduction of vortex lines through the sample in one of the systeretic state, equilibrium state where vortices are penetrated through the sample, while the excited state rejects external vortices.

Hysteretic behavior is known for some of the type II superconductors as the de Gennes, Bean & Lipingston effect [9], where surface barrier makes the sample diamagnetic just in the similar manner as in the Meissner state.

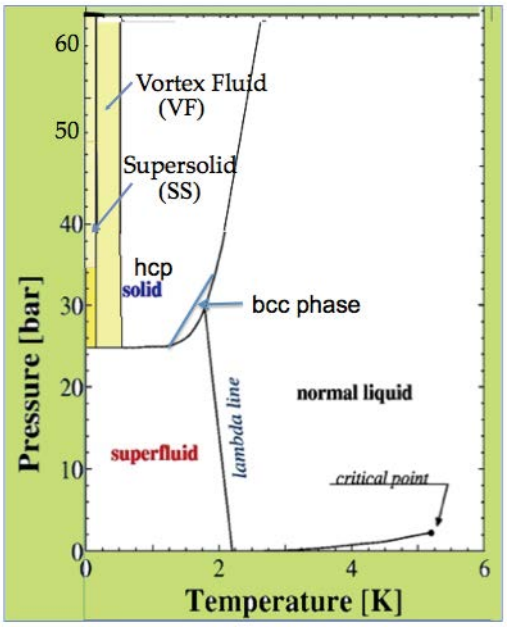

Fig. 1. *P-T* phase diagram of ^{4}He deduced from the TO measurements. The vortex fluid (VF) state continues to T = 0K from the onset temperature T_o ~ 500 mK, while the supersolid (SS) state appears below T_c =~75 mK.

References
[1] O. Penrose and L. Onsager, Phys. Rev. **104**, 576 (1956).
[2] G. V. Chester, Phys. Rev. A **2**, 256 (1970); A. F. Andreev and I. M. Lifshitz, JETP **29**, 1107 (1969); A. J. Leggett, Phys. Rev. Lett. **25**, 1543 (1970).
[3] E. Kim & M. H. W. Chan, NATURE **427**, 225 (2004); Science **305**, 1941 (2004).
[4] See for the reviews till 2007 or 2008; N. Prokof'ev, Adv. Phys. **56(2)**, 381 (2007); S. Balibar and F. Caupin, J. Phys.: Condens. Matter **20**, 173201 (2008); D. Galli and L. Reatto, J. Phys. Soc. Jpn. **77(11)**, 111010 (2008).
[5] M. Fukuda, M.K. Zalalutdinov, V. Kovacik, T. Minoguchi, T. Obata, M. Kubota, and E. B. Sonin, Phys. Rev. B **71**, 212502 (2005).
[6] P. W. Anderson, Nature Physics **3**, 160 (2007)
[7] M. Yagi, A. Kitamura, N. Shimizu, Y. Yasuta, and M. Kubota, J. Low Temp. Phys. **162**, 492 (2011); ibid, **162**, 754.
[8] M. Kubota, submitted to J Low Temp Phys, special issue on solid He (2012); arXiv:1203.6824. see also references in it.
[9] De Gennes, "*Superconductivity in Metals and Alloys*", Benjamin, (Frontiers in physics series); Lecture notes from a course given in the Faculty sciences, Orsay, France, 1962-63, 76 (1965); C.P. Bean and J.D. Livingston, Phys. Rev. Lett. **12**, 14 (1964).

Authors
M. Kubota, M. Yagi, N. Shimizu, K. Rogacki[a], A. Kitamura[b], and S. Harada[b]
[a]Inst. Low Temp. & Struc. Research,Wroclaw, Poland
[b]Niigata University

Experimental Confirmations of Dirac Fermions and Helical Suface State in an Organic Zerogap Conductor

Osada Group

It has been theoretically predicted that the quasi-2D massless Dirac fermion system is realized in a layered organic conductor α-(BEDT-TTF)$_2$I$_3$ under high pressures. By transport and thermodynamic measurements, we have obtained the experimental proofs of realization of Dirac fermions and a novel surface state at the high-field quantum limit.

(1) Density of states of Dirac fermions

The temperature dependence of the specific heat shows almost quadratic behavior at low temperature, suggesting linear energy dispersion in this system. In a magnetic field, the specific heat increases as the field increases, and then turns to decrease in high field (Fig. 1). This behavior can be understood by assuming the n=0 Landau level (LL), so-called zero-mode, characteristic of the Dirac fermion system; In perpendicular magnetic field above 0.2 T, the α-(BEDT-TTF)$_2$I$_3$ is in the quantum limit, where only the zero-mode exists at Fermi energy E_F. The density of states (DOS) of the zero-mode increases in proportion to the magnetic field, reflecting the LL degeneracy. In addition, each LL splits as $2\mu_B B$ in the magnetic field because of the Zeeman effect (spin splitting). As a result, the DOS at E_F first increases with magnetic field, and then starts to decrease in a high magnetic field when the spin splitting becomes larger than the LL broadening. These results are quite consistent with the reported magnetoresistance. When we take into account the field dependence of the LL broadening width $\Gamma \propto B^{1/2}$ predicted in the self-consistent Born approximation, we can fit our data satisfactorily by using the Gaussian shaped LL (broken line in Fig. 1).

(2) Surface transport due to helical surface state

The ν=0 quantum Hall (QH) state can be expected in the field range where the spin splitting of the n=0 LL becomes sufficiently large. In this situation, a pair of QH edge channels with opposite spin and chirality must be formed along the edge on each layer. The interlayer tunneling couples these edge states on different layers, resulting in the formation of the "helical surface state" surrounding the edge surface (Fig. 2(a)). The helical surface state contributes to metallic surface transport, which becomes dominant contribution to interlayer transport at high fields and low temperatures where activated bulk transport becomes exponentially small. We have proposed this scenario to explain the observed saturation of the interlayer magnetoresistance.

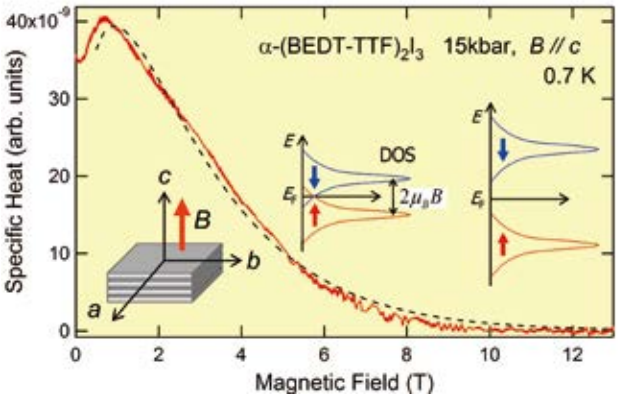

Fig. 1. Field dependence of specific heat at 15kbar. The decrease of the specific heat means the decrease of DOS at the Fermi level. It is an evidence of spin splitting of the n=0 LL.

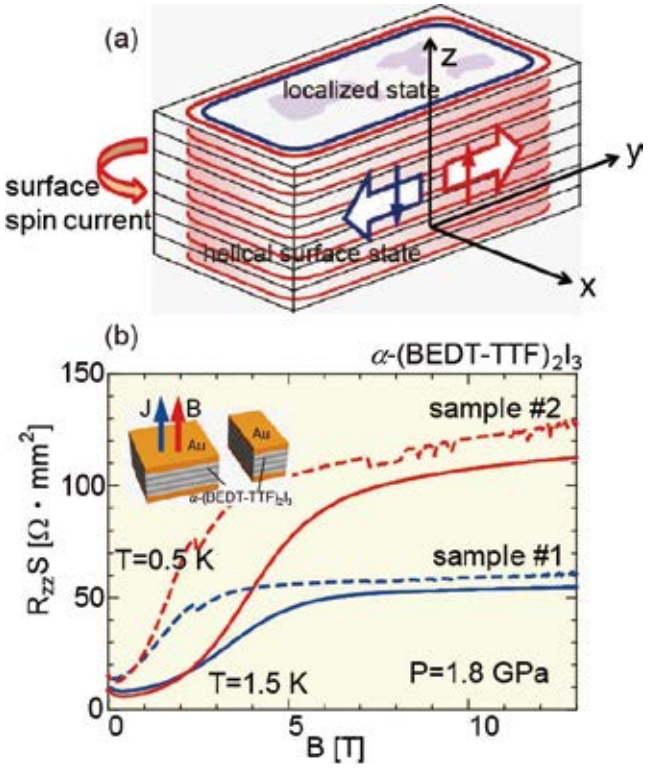

Fig. 2. (a) Helical surface state in the ν=0 QH state in a Dirac multilayer. (b) Interlayer magnetoresistance scaled by cross sectional area of two samples prepared by cutting one crystal. Their mismatch in the saturation region is an evidence of non-uniform conduction.

To confirm the existence of the helical surface state, we have experimentally studied the saturation feature as a function of the cross sectional area and the perimeter of samples. As shown in Fig. 2(b), the interlayer magnetoresistance is well scalled by the sectional area, indicating the bulk uniform conduction, in low field region. However, the high-field saturation is never scaled by the cross sectional area, indicating the non-uniform transport such as surface transport. The strong correlation between the saturated value and the sample perimeter strongly suggests the surface transport due to the helical surface state.

Authors
T. Osada, T. Konoike, M. Sato, and K. Uchida

Heat Capacity Measurement of Heavy Fermion Compound $YbCo_2Zn_{20}$ under Magnetic Field

Uwatoko Group

Recently, one of the most interesting topics has been the ground state properties of heavy fermion compounds located close to a magnetic Quantum Critical Point (QCP). Applying pressure or magnetic field controls the electronic configuration, and thus anomalous behaviors appear at around magnetic QCP, such as an unconventional superconductivity and non-Fermi liquid state. In the case of Yb based heavy fermion compounds, it is known that $YbCo_2Zn_{20}$ is a prototypical compound of the pressure-induced QCP from a paramagnetic state to an antiferromagnetic. The high temperature magnetic susceptibility shows the Curie-Weiss law with

the effective moment close to the value of Yb^{3+} (μ_{eff} = 4.5 μ_B), although there is no indication of magnetic order down to 20 mK. The low temperature electrical resistivity and specific heat follows $\rho = \rho_0 + AT^2$ and C/T = const : which indicates the Fermi-liquid behavior: the values of A and γ are 165 Ωcm/K^2 and 7900 mJ/moleK^2, respectively. These large values of A and γ are due to the small Kondo temperature, suggesting the closeness to the pressure induced magnetic order. According to the resistivity, specific heart and neutron diffraction measurements under pressure, magnetic ordered phase appears around critical pressure P_c = 1 GPa. Figure 1 shows the pressure phase diagram of $YbCo_2Zn_{20}$ [1]. The applying pressure stabilizes the magnetic Yb^{3+} configuration and resulting in the appearance of a magnetically ordered state. It is worth noting that the critical pressure of $YbCo_2Zn_{20}$ is lower than that of other Yb based compounds such as $YbNi_2Ge_2$ (P_c = 5 GPa) and $YbCu_2Si_2$ (P_c = 8 GPa). Therefore $YbCo_2Zn_{20}$ has an advantage of investigating the behavior of Yb based compounds near QCP.

More interestingly, it is reported that a metamagnetic crossover occurs at H_m ~ 0.57 T by M. Ohya *et al*. The origin of this metamagnetic behavior is not fully understood, however relevance to the valence fluctuation is considered by S. Watanabe and K. Miyake. To shed light on the nature of the metamagnetic behavior, the specific heat of $YbCo_2Zn_{20}$ single crystal under magnetic field has been measured at ambient pressure. Figure 2 shows the temperature dependence of the electronic contribution of the specific heat C_e/T under magnetic field on a logarithmic temperature scale. At zero- field, C_e/T exhibits a broad shoulder structure at around 2 K due to the combined effect of the Kondo effect and the Schottky anomaly associated with the crystalline electronic field (CEF) splitting. With increasing magnetic field, the T_{FL} is gradually suppressed to a lower temperature. It is worth noting that C_e/T diverges more rapidly than a logarithmic dependence at H_m ~ 0.6 T, which corresponds to the metamagnetic field. With further increasing magnetic field, the temperature dependence changes to a peak structure

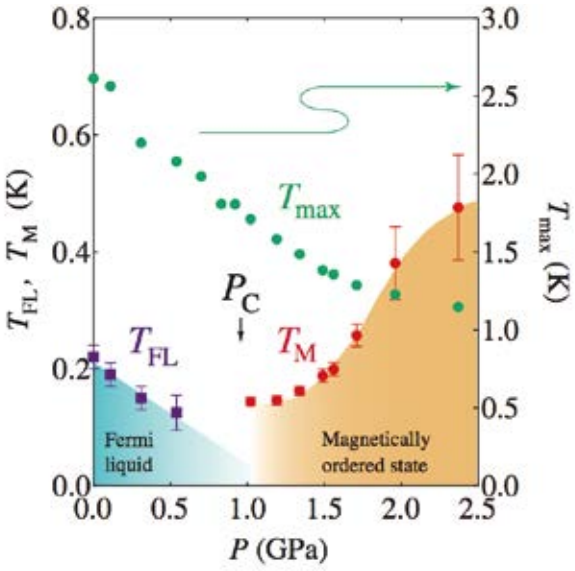

Fig. 1. Pressure–temperature phase diagram of $YbCo_2Zn_{20}$. T_{max} and T_{FL} are suppressed by applying pressure, and thus, the nonmagnetic Fermi-liquid state vanishes around P_c. T_M appears to abru ptly develop above P_c, where T_{max} decreases. Assuming that the observed T_{max} in the resistivity is proportional to T_K, the value of T_K decreases with an increase in the pressure. According to a theoretical study, the suppression of valence fluctuations leads to a decrease in T_K. It is generally accepted that the magnetic instability results from the competition between the RKKY and the Kondo interactions. By applying pressure, the RKKY interaction becomes more dominant with a reduction in the Kondo interaction.

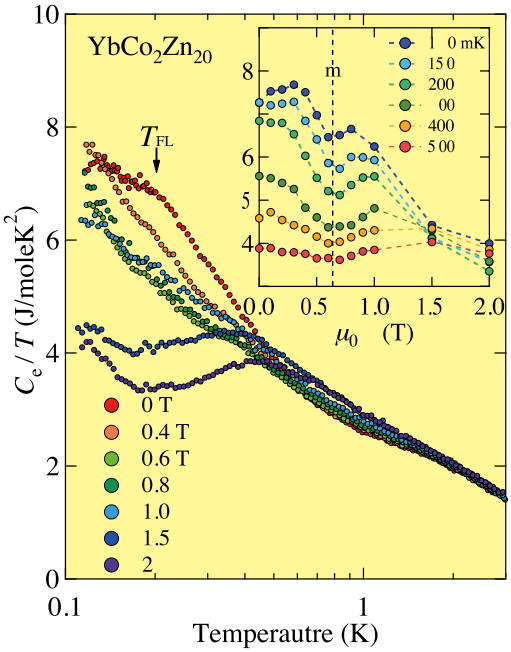

Fig. 2. Temperature dependence of the electronic contribution of the specific heat for $YbCo_2Zn_{20}$ at selected magnetic field (H // [110]). Arrow indicates the onset temperature of the Fermi liquid behavior. Here, the electronic contribution to the specific heat C_e of $YbCo_2Zn_{20}$ was obtained by subtracting that of $LuCo_2Zn_{20}$. At lower temperature, C_e/T increases logarithmically and tends to saturate below T_{FL} ~ 0.2 K, coinciding with the T^2 dependence in the resistivity, namely Fermi-liquid behavior as observed in the previous report. Inset : Field dependence of C_e/T at selected temperature. Two peak structure, which has local minimum point at H_m, was observed at around 0.6 T.

as typical behavior of Kondo systems under magnetic field. C_e/T as a function of magnetic field at selected temperature has been plotted to see the field variation in inset of fig. 2. The most intriguing feature obtained here is the two peak structure which has local minimum point at H_m ~ 0.6 T. Although the double peak structure becomes weaker with increasing temperature, the minimum point is temperature independent. Similar feature is also observed in the prototypical heavy fermion compound $CeRu_2Si_2$ which shows metamagnetic transition at H_m ~ 7.7 T by J. Flouquet *et al*. In the case of $CeRu_2Si_2$, the field dependence of C_e/T exhibits the double peak structure above 1 K, and thus that changes to a single peak structure at lower temperatures. Here we compare the characteristic energy scales of $YbCo_2Zn_{20}$ to those of $CeRu_2Si_2$. It is obvious that the values of H_m and T_{max} of $YbCo_2Zn_{20}$ are ten times smaller than that of $CeRu_2Si_2$, i.e. the characteristic energy scale of $YbCo_2Zn_{20}$ is much smaller than that of $CeRu_2Si_2$. Considering the difference of the energy scale, it is expected that the double peak structure in $YbCo_2Zn_{20}$ may evolve into a single peak structure at lower temperature, suggesting the development of the critical fluctuation. Further experimental and theoretical studies are needed to clarify the origin of the metamagnetic behavior and the relationship with the pressure-induced magnetically ordered state of $YbCo_2Zn_{20}$.

Reference

[1] Y. Saiga, K. Matsubayashi, T. Fujiwara, M. Kosaka, S. Katano, M. Hedo, T. Matsumoto and Y. Uwatoko, J. Phys. Soc. Jpn. **77**, 053710 (2008).

Authors

R. Yamanaka, K. Matsubayashi, Y. Saiga[a], T. Kawae[b], and Y. Uwatoko
[a]Hiroshima University
[b]Kyushu University

Quantitative Waveguide Absorption Spectroscopy of Nano-Structures

Akiyama Group

New absorption-spectroscopy methods that utilize internal photoluminescence light as a source for probe light are developed, and used to measure the quantitative absorption spectra of quantum wires and a single quantum well embedded in an optical waveguide.

By applying this method to two-dimensional excitons in an un-doped 8 nm GaAs/AlAs single quantum well, we characterized possible errors and accuracy of this method. In addition, we compared the measured absorption spectra with photoluminescence-excitation (PLE) spectra. It was found that the lowest exciton peak in the PLE spectra at low temperatures was deviated from that in the absorption spectra. This effect was attributed to the de-excitation via resonant-Rayleigh-scattering processes, which has been known as the Heitler effect.

We also applied this method to one-dimensional (1D) excitons in T-shaped quantum wires, as shown in Fig. 1, and evaluated the modal absorption area of the 1D ground-state excitons as 0.39 eV cm^{-1}, which was almost independent of temperature in the range 4–150 K. This revealed that the absorption cross-section per unit length at resonance peak and the spectrally integrated absorption cross-section area per unit length of the 1D ground-state excitons were 1.0 nm and 2.5 × 10^{-3} eV nm, respectively. We confirmed that this value is consistent with the intrinsic radiative lifetime of 1D excitons evaluated separately.

References

[1] T. Mochizuki *et al.*, Jpn. J. Appl. Phys. (to be published).

[2] M. Yoshita *et al.*, Appl. Phys. Lett. **100**, 112101 (2012).

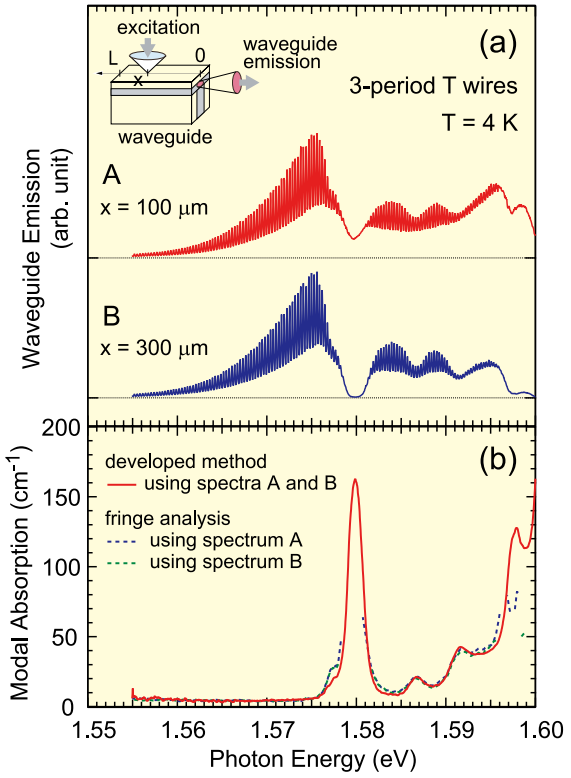

Fig. 1. (a) Waveguide-emission spectra of 3-period T wires embedded in T-shaped optical waveguide at 4 K under point photoexcitation at x=100 and 300 μm from cavity edge. Inset shows schematic view of experimental configuration. (b) Absorption spectra derived from waveguide-emission spectra shown in (a) using developed analysis method (solid line) and using Fabry–Pérot fringe analysis (dotted lines).

Authors

T. Mochizuki, M. Yoshita, C. Kim, S. Chen, S. Maruyama, K. Fukuda, H. Akiyama, L. N. Pfeiffer[a], and K. W. West[a]

[a]Princeton University, USA

Hydrogen-induced Surface Metallization of $SrTiO_3$(001)

I. Matsuda Group

Transition-metal oxides, especially the perovskite-type, have been extensively studied in the past decades. Recently, their surface/interface systems have obtained great interests since the discovery of a two-dimensional electron gas (2DEG) at the interface of the two insulating oxides $LaAlO_3$ and $SrTiO_3$ [1]. It has been predicted by *ab initio* calculations that hydrogen adsorption on a SrO or TiO_2 terminated $SrTiO_3$(001) surface leads to a metallic state at the surface [2]. Such H-induced metallization was already reported for H/ZnO [3] crystal surfaces. In the case of $SrTiO_3$ surface, the metallicity is assigned to the bulk band-bending near the surface, where the bulk conduction band is filled with electrons donated from the H atoms adsorbed on the surface. As hydrogen adsorption on a crystal surface prepared under UHV is a well-controlled procedure, experimental examination of the H-induced metallization of a $SrTiO_3$(001) surface is thus strongly called for.

In the present research[4], we examined the hydrogen-induced surface metallization on the H/$SrTiO_3$(001) system. The electronic structure of the clean and H-adsorbed

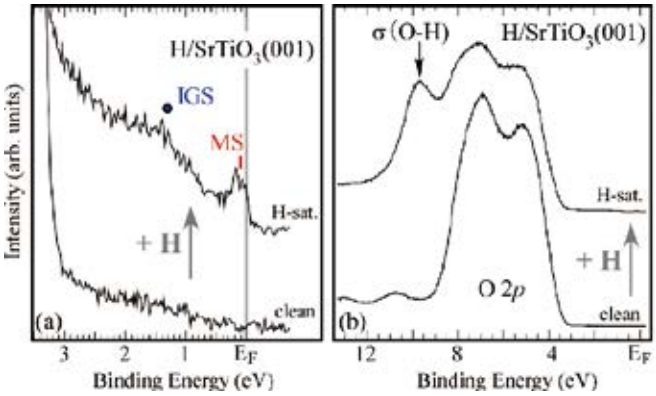

Fig. 1. Normal-emission photoemission spectra of the bare and the H-saturated $SrTiO_3$(001) surfaces (a) at the Fermi level (E_F) and (b) at the O 2*p* band. Spectra were taken at hv=81eV and at room temperature.

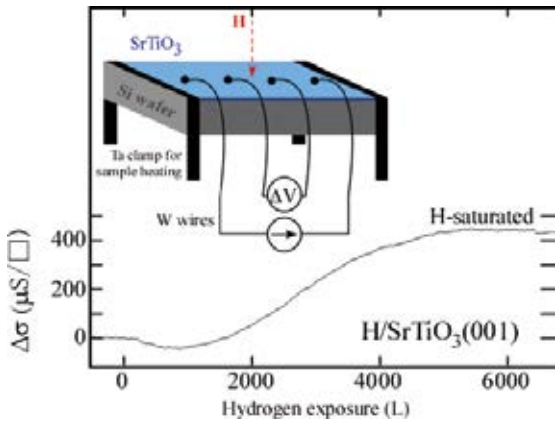

Fig. 2. Conductivity change, Δσ, with H exposure, referred to the conductivity of the clean surface. Measurements were performed at room temperature. (Inset) Schematic of four-terminal method transport measurements on the H/$SrTiO_3$(001) surface.

$SrTiO_3$(001) surfaces is investigated by core-level and valence band photoemission spectroscopy measurements at the TEMPO beamline, SOLEIL, France, and SPring-8 BL07LSU[5]. Electrical conductivity is measured *in situ* during H-exposure by the four terminal method under UHV conditions with linearly aligned four probes. We found a dispersing metallic band and an increase of the surface conductivity after H adsorption. The metallic state (MS) is assigned to a quantized state in the space charge layer near the surface. The MS photoemission peak was associated with broad spectral features of the many-body effect. After the metallization, an electronic state in the bulk band gap (in-gap state, IGS) and a state, assigned to the O-H bond, were also observed. The measured two-dimensional (2-D) conductivity exceeds the 2-D Ioffe-Regel limit, indicating band conduction regime, and the mean free path of surface electrons is estimated to be several nm at room temperature.

References

[1] A. Ohtomo, D. A. Muller, J. L. Grazul, and H. Y. Hwang, Nature **419**, 378 (2002).
[2] F. Lin, S. Wang, F. Zheng, G. Zhou, J. Wu, B.-L. Gu, and W. Duan, Phys. Rev. B **79**, 035311 (2009).
[3] K. Ozawa and K. Mase, Phys. Rev. B **81**, 205322 (2010).
[4] M. D'Angelo, R. Yukawa, K. Ozawa, S. Yamamoto, T. Hirahara, S. Hasegawa, M.G. Silly, F. Sirotti, and I. Matsuda, Phys. Rev. Lett. **108**, 116802 (2012).
[5]M. Ogawa, S. Yamamoto, Y. Kousa, F. Nakamura, R. Yukawa, A. Fukushima, A. Harasawa, H. Kondo, Y. Tanaka, A. Kakizaki, and I. Matsuda, Rev. Sci. Instrum. **83**, 023109 (2012).

Authors

M. D'angelo[a], R. Yukawa, K. Ozawa[b], S. Yamamoto, T. Hirahara, S. Hasegawa, M.G. Silly[c], F. Sirotti[c], and I. Matsuda
[a]Institut des Nanosciences de Paris, Universit´e Pierre et Marie Curie-Paris 6, France
[b]Tokyo Institute of Technology
[c]TEMPO Beamline, Synchrotron Soleil, France

Metal-Insulator Transition and Charge Order under Pressure in Vanadium Hollandite

Y. Ueda Group

Metal-insulator transition (MIT) is one of the most drastic phenomena in strongly correlated electron systems. The most remarkable property of binary vanadium oxides is MIT as a function of temperature. The MITs in mixed valent binary vanadium oxides are characterized by charge order and formation of spin singlet V^{4+}-V^{4+} pairs. We found a MIT at 170 K in a ternary vanadium oxide; hollandite $K_2V_8O_{16}$. This MIT is accompanied by a sudden jump of resistivity and reduction of magnetic susceptibility [1]. The structure changes from a tetragonal structure for the high-temperature (HT) metallic phase to a monoclinic structure for the low-temperature (LT) insulating phase. The unit cell of LT phase becomes as large as $\sqrt{2} \times \sqrt{2} \times 2$, suggesting charge order and formation of V-V pairs. Recently we succeeded in determining crystal structure of LT phase [2]. The structure of $K_2V_8O_{16}$ consists of a tubular V_8O_{16} framework and K ions (see the inset in Fig. 1). The V_8O_{16} framework is built up by bridging double chains (zigzag chains) made of edge-sharing VO_6 octahedra via oxygen atoms. The V site is unique in HT phase. Hence, the compound has a uniform and average valence of $V^{+3.75}$ (V^{3+}/V^{4+} = 1/3). In LT phase (CO1), on the other hand, charge segregation and order yield two types of double chains; V^{4+}-V^{4+} double chain and V^{3+}-V^{4+} double chain. These double chains are arranged

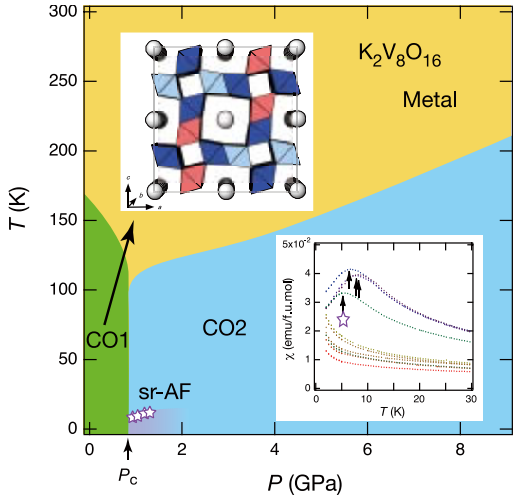

Fig. 1. *P-T* phase diagram of $K_2V_8O_{16}$. $K_2V_8O_{16}$ shows a metal-insulator transition at 170 K under ambient pressure, accompanied by charge order and formation of spin singlet V^{4+}-V^{4+} pairs. The charge ordered manner of this insulating phase (CO1) is shown in the upper inset. The V_8O_{16} framework consists of two types of double chains: one is formed by $V^{3+}O_6$ chain (red) and $V^{4+}O_6$ chain (deep blue) and the other is formed by only $V^{4+}O_6$ chains (deep blue and sky blue). V^{3+}-V^{3+} pairs and V^{4+}-V^{4+} pairs are formed along the *b*-axis in $V^{3+}O_6$ chain (red) and $V^{4+}O_6$ chain (sky blue), respectively, resulting in the dimerization along the *b*-axis. The transition temperature is once suppressed by pressure and then turns to increase beyond the critical pressure $P_c \sim 1$ GPa. This means the appearance of a new insulator phase (CO2) above P_c. The lower inset shows magnetic susceptibility curves under various pressures. They suddenly change beyond P_c; they are almost temperature independent below P_c, while above P_c they have maximums around 7 K, indicating the development of short range antiferromagnetic order (sr-AF).

in a manner shown in the upper inset in Fig. 1, resulting in an inplane supercell of $\sqrt{2} \times \sqrt{2}$. Furthermore, half of the double chains are dimerized by forming V^{3+}-V^{3+} pairs in the V^{3+}-V^{4+} double chains and V^{4+}-V^{4+} pairs in the V^{4+}-V^{4+} double chains, resulting in the doubling of the *b*-axis (tunnel direction). These V pairs perfectly explain the reduction of magnetic susceptibility due to the formation of spin singlets. The remained unpaired V^{4+} chains, which would have a much larger intra-chain antiferromagnetic exchange interaction than 170 K, are responsible for the considerable and temperature-independent magnetic susceptibility in LT phase.

The MIT in $K_2V_8O_{16}$ is accompanied by a volume increase in LT phase. Actually the MIT is suppressed by hydrostatic pressure, but unexpectedly the transition temperature turns to increase beyond the critical pressure $P_c \sim 1$ GPa [3], as shown in Fig. 1. This indicates the emergence of new charge ordered phase (CO2) beyond P_c. The magnetic susceptibility clearly shows the appearance of a new phase with a different electronic state. As shown in the lower inset in Fig.1, the magnetic susceptibilities are almost temperature independent below P_c, while above P_c the magnetic susceptibility curves have maximums around 7 K. The lack of long range magnetic order was confirmed from NMR. Hence, such maximums correspond to the development of short range order in one-dimensional magnetic chains. $K_2V_8O_{16}$ has a formal valence of $6V^{4+}$ and $2V^{3+}$ and has 10 *d* electrons in an f.u. The Curie constants estimated from Curie-Weiss fitting of magnetic susceptibility correspond to 2 *d* electrons in an f.u. above P_c, assuming spin-1/2. This suggests that magnetic V ions in a fraction about 1/5 are arranged in a low dimensional manner and are weakly coupled. The manner of charge ordering and pairing has remained unsolved.

References

[1] M. Isobe, S. Koishi, N. Kouno, J. Yamaura, T. Yamauchi, H. Ueda, H. Gotou, T. Yagi, and Y. Ueda, J. Phys. Soc. Jpn. **75**, 073801 (2006).

[2] A. C. Komarek, M. Isobe, J. Hemberger, D. Meier, T. Lorenz, D. Trots, A. Cervellino, M. T. Fernández-Díaz, Y. Ueda, and M. Braden, Phys. Rev. Lett. **107**, 027201 (2011).
[3] T. Yamauchi, H. Ueda, M. Isobe, and Y. Ueda, Phys. Rev. B **84**, 115104 (2011).

Authors
Y. Ueda, M. Isobe, and T. Yamauchi

Orbital Switching Transition in a Quasi-Kagomé Antiferromagnet Volborthite

Hiroi Group

Kagomé antiferromagnets have been extensively studied to search for exotic magnetic phenomena. It is believed that an unknown ground state, such as a spin-liquid, is realized instead of the conventional Néel order due to strong geometrical frustration for spins residing on the kagomé lattice. Several Cu minerals comprising kagome lattices made up of Cu^{2+} ions have been focused thus far as model compounds for the spin-1/2 kagome antiferromagnet: herbertsmithite $ZnCu_3(OH)_6Cl_2$, volborthite $Cu_3V_2O_7(OH)_2 \cdot 2H_2O$, vesignieite $BaCu_3V_2O_8(OH)_2$, haydeeite $Cu_3Mg(OH)_6Cl_2$, and kapellasite $Cu_3Zn(OH)_6Cl_2$. However, the true ground state of the spin-1/2 kagome antiferromagnet remains still mystery because of some obstacles in real compounds: distortion, defects and other deviations from the ideal kagomé model tend to hinder the characterization of low-temperature magnetic properties.

Volborthite is a mineral found in nature as yellow-green crystals of sub-millimeter size. A decade ago, the compound was first studied in terms of kagomé physics [1]. Recently, a high-quality powder sample of volborthite was synthesized in a hydrothermal condition and found to exhibit anomalous magnetic transitions at very low temperatures around 1 K and also under high magnetic fields [2, 3]. The compound crystallizes in a monoclinic structure with space group *C*2/*m* (Fig. 1). The kagomé layer consists of edge-sharing CuO_6 octahedra and is separated by non-magnetic V_2O_7 pillars and water of crystallization. There are two crystallographic sites for Cu; the Cu1 and Cu2 atoms are arranged in isosceles triangles with approximately 3% distortion, which are connected to each other to form a slightly distorted kagomé plane. It is obvious from the deformations of the CuO_6 octahedra that the unpaired electrons on Cu1 and Cu2 occupy $d_{3z^2\text{-}r^2}$ and $d_{x^2\text{-}y^2}$ orbitals, respectively.

Very recently, we found a unique structural transition at around room temperature that shows "switching" from one *d* orbital to another upon cooling in a synthetic single crystal of volborthite [4]. The transition causes a large change in the coordination environment of the Cu1 site: the $Cu1O_6$ octahedron takes two short Cu-O bonds and four long bonds in the high-temperature (HT) phase (space group *C*2/*m*), while two long and four short bonds in the low-temperature (LT) phase (*I*2/*a*). This means that the $d_{x^2\text{-}y^2}$ orbital must be selected in the LT phase, instead of the $d_{3z^2\text{-}r^2}$ orbital in the HT phase. On the other hand, there is little change in the coordination of Cu2 with the spin-carrying orbital unchanged.

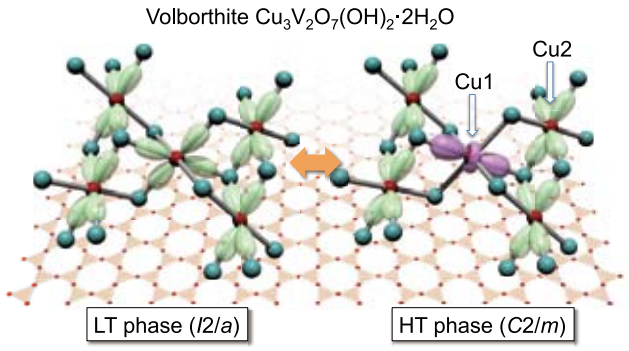

Fig. 1. Orbital switching transition observed in a single crystal of volborthite. Parts of the kagomé layer of the HT phase (right) and the LT phase (left) are illustrated. In the HT phase, $d_{3z^2\text{-}r^2}$ and $d_{x^2\text{-}y^2}$ orbitals are selected for spins at the Cu1 and Cu2 sites, respectively. In contrast, $d_{x^2\text{-}y^2}$ orbitals are selected at all the Cu sites in the LT phase, indicating that orbital switching takes place at the Cu1 site.

The change in the orbital state found in volborthite should be distinguished from the phenomenon known as orbital ordering. In general, orbital order occurs in systems where the symmetry of the coordination polyhedra is high, leading to orbital degeneracy and thus an orbitally disordered ground state. This symmetry may be broken, and a unique orbital configuration is selected by a cooperative Jahn-Teller distortion at lower temperatures, as observed in $NaNiO_2$ (Ni^{3+}, d^7). This is an order-disorder transition associated with the orbital degree of freedom. In contrast, because of the strong Jahn-Teller effect of the Cu^{2+} ion, no corresponding orbital disordered state has been observed in any copper compounds even at high temperature; most compounds decompose before orbital disordering. Therefore, the change in the orbital state in volborthite is not orbital order, but could be called orbital switching.

Because magnetic interactions between Cu spins in the kagomé lattice are seriously modified by the orbital switching, magnetic properties of the compound change dramatically. Magnetic long-range order occurs through two successive phase transitions at around 1 K in single crystals, which differs from the previously reported LT behavior of polycrystalline samples. Detailed investigations are now in progress.

References
[1] Z. Hiroi, N. Kobayashi, M. Hanawa, M. Nohara, H. Takagi, Y. Kato, and M. Takigawa, J. Phys. Soc. Jpn. **70**, 3377 (2001).
[2] H. Yoshida, Y. Okamoto, T. Tayama, T. Sakakibara, M. Tokunaga, A. Matsuo, Y. Narumi, K. Kindo, M. Yoshida, M. Takigawa, and Z. Hiroi, J. Phys. Soc. Jpn. **78**, 043704 (2009).
[3] M. Yoshida, M. Takigawa, H. Yoshida, Y. Okamoto, and Z. Hiroi, Phys. Rev. Lett. **103**, 077207 (2009).
[4] H. Yoshida, J. Yamaura, M. Isobe, Y. Okamoto, G. J. Nilsen, and Z. Hiroi, Nat. Commun. **3**, 860 (2012).

Authors
H. Yoshida[a], J. Yamaura, M. Isobe[a], Y. Okamoto, G. J. Nilsen, and Z. Hiroi
[a]National Institute for Materials Science

High-performance Ion Gel

Shibayama Group

Polymer electrolytes using room-temperature ionic liquids (ILs) occupy an important position in the field of solid-state ionics, as well as those containing high-melting temperature salts and/or hard inorganic solid electrolytes. The ILs possess unique properties such as high ionic conductivity, negligible volatility and high thermal stability, therefore, electrochemical research has been performed to explore a new class of electrolytes in device developments. Though many researchers have proposed use of ILs for polymerization solvents and also reported the ionic conductivity of the prepared IL-polymer electrolytes (ion gels), the ionic

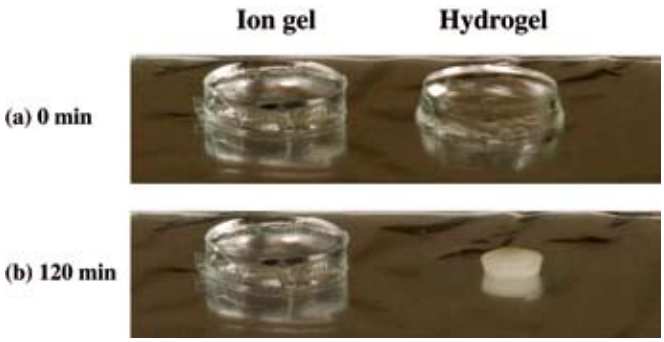

Fig. 1. Photographs of Tetra-PEG ion gel (left) and Tetra-PEG hydrogel (right) showing the difference in the stability against heat. Both gels were placed on a hot plate at 100 °C. By time went from 0 min (a) to 120 min (b), the hydrogel was completely dried, while the ion gel remain as it had been.

conductivity decreases at least one order relative to that of the corresponding pure IL. This is because high polymer content is necessary to obtain a free-standing ionic liquid/polymer electrolyte.

We succeeded in preparation of ion gels consisting of imidazolium-based ionic liquids and Tetra-PEG network [1]. Here, Tetra-PEG denotes tetra-arm poly(ethylene glycol). Hereafter, we call the obtained polymer gel "Tetra-PEG ion gel". The Tetra-PEG ion gel was prepared by mixing two Tetra-PEG macromers in ILs at room temperature. The polymer concentrations were 3 and 6 wt%. The preparation of Tetra-PEG gel is reported elsewhere [2]. The ILs examined were 1-ethyl-3-metylimidazolium bis(trifluoromethanesulfonyl)amide, [C_2mIm$^+$][TFSA$^-$] and 1-ethyl-3-metylimidazolium bis(fluorosulfonyl)amide, [C_2mIm$^+$][FSA$^-$]. Fig. 1 shows time-course of photographs of Tetra-PEG ion gel (left) and hydrogels (right) placed on an electric hot plate (a) 0 min and (b) after 120 min. The surface temperature of the hot plate was 100 °C. As shown in the figure, Tetra-PEG ion gel did not change at all, while Tetra-PEG hydrogel was dried completely within 120 min. Fig. 2 shows the ionic conductivities, σ, for 3 and 6 wt% Tetra-PEG ion gels. The obtained values of σ are very close to that of pure solvent, i.e., [C_2mIm$^+$][TFSA$^-$]. At room temperature, the σ values are 8.5 and 7.7 × 10^{-3} S cm^{-1} for 50 and 100 mg/ml Tetra-PEG ion gels, respectively, which are much higher than the values already reported for conventional polymer electrolytes. As seen in this figure, the σ value slightly decreases with increasing Tetra-PEG concentration.

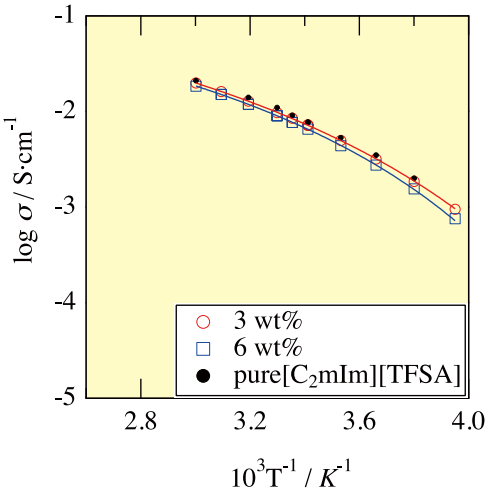

Fig. 2. Temperature dependence of ionic conductivity for 3 (red circles with line) and 6 wt% (blue squares with line) Tetra-PEG ion gels containing [C_2mIm$^+$][TFSA$^-$] (red and blue, respectively), together with that for pure IL (black dots). The solid lines show the fitting curve with VFT equation.

However, the σ value at higher concentrations remained 85% of pure IL (9.1 × 10^{-3} Scm^{-1}). The experimental data were well represented by the Vogel-Tamman-Fulcher (VTF) equation for conductivity for such electrolytic materials, which is shown by solid lines in Figure 2. The VFT equation is given by $\sigma = \sigma_0 \exp[-B/(T - T_0)]$ where σ_0, B and T_0 are adjustable parameters. The mechanical properties were examined by stretching as well as compression measurements and it was found that the ion gels are strong enough to be used as a free-standing electrolyte. Uniformity of the network structure of Tetra-PEG ion gels was confirmed by small-angle neutron scattering.

A free-standing ion gel with high strength and toughness was obtained by directly cross-end-coupling of two Tetra-PEG macromer (3.2 and 6.4 wt%) in room temperature ionic liquid. The ionic conductivity is practically equal to that of pure IL. The mechanical properties of Tetra-PEG ion gels are comparable to those of high-strength Tetra-PEG hydrogels [3].

References

[1] K. Fujii, H. Asai, T. Ueki, T. Sakai, S. Imaizumi, U. Chung, M. Watanabe, and M. Shibayama, Soft Matter **8** (2012).
[2] T. Sakai, T. Matsunaga, Y. Yamamoto, C. Ito, R. Yoshida, S. Suzuki, N. Sasaki, M. Shibayama, and U. I. Chung, Macromolecules **41** (2008).
[3] H. Asai, K. Fujii, T. Ueki, T. Sakai, U. Chung, M. Watanabe, Y. S. Han, T. H. Kim, and M. Shibayama, Macromolecules **45** (2012).

Authors

K. Fujii, H. Asai, T. Ueki, T. Sakai, U. Chung, M. Watanabe[a], and M. Shibayama

[a]Yokohama National University

Structure and Dynamics of Domains in Imidazolium-based Ionic Liquids

Yamamuro Group

Ionic liquids (ILs) are ionic compounds whose melting temperatures are around or lower than room temperature. The cations of ILs are alkylimidazolium, alkylprydinium, alkylammonium, etc., which consist of core parts with positive electric charges and alkyl-chains with hydrophobic interactions. On the other hand, halogen ions and many ionic groups, *e.g.*, BF_4^-, PF_6^-, $(CF_3SO_3)^-$, $(CF_3SO_2)_2N^-$, can be the anions of ILs. ILs have various useful properties as green solvents and electrochemical materials, *e.g.*, low vapor-pressure, non-combustivity, high electric conductivity, etc. ILs have therefore been investigated mainly from the inter-

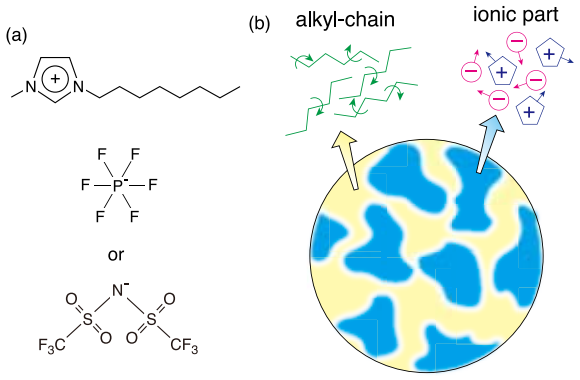

Fig. 1. Schematic drawings of (a) ionic structures of C8mimPF6 and C8mimTFSI, and (b) their domain strictures.

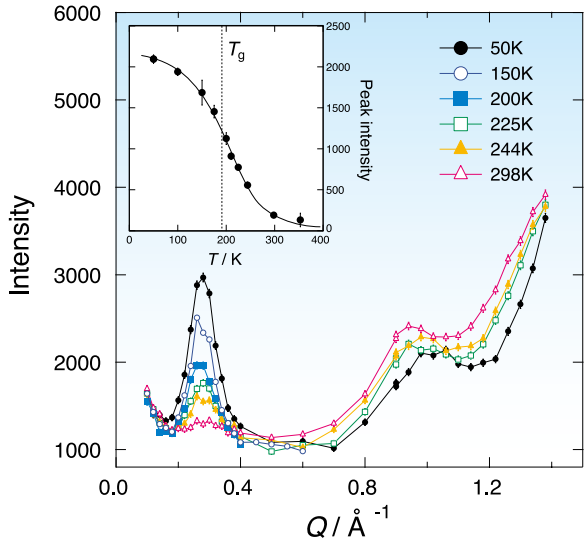

Fig. 2. Neutron diffraction data of C8mimPF6. The inset shows the temperature dependence of the intensity of the peak at 0.3 Å^{-1}.

ests of application and industry. However, the basic physical properties of ILs, especially at low temperatures, have not been studied well. The most characteristic feature of ILs is the formation of domain structures as shown in Fig.1(b); ionic domains consisting of polar parts (imidazolium rings) of cations and anions and neutral domains of alkyl-chains of cations. The domain structure may play key roles for various interesting properties of ILs, *e.g.*, stability of undercooled state, high fragility, non-Einstein-Stokes dynamics, etc. The purpose of this study is to clarify the structure and dynamics of the domains of imidazolium-based ILs.

We have performed neutron diffraction and spin echo experiments on 1-octyl-3-methylimidazolium hexafluorophosphate (C8mimPF$_6$) and 1-octyl-3-methylimidazolium bis(trifluoromethanesulfonyl) imide (C8mimTFSI), whose ionic structures are shown in Fig.1(a), using an NSE instrument at NCNR, NIST (USA). This instrument with using the wavelength of 6 Å can provide relaxation data in the Fourier time region of 6 ps to 17.5 ns. These two samples were chosen since clear domain structures and relatively fast domain motions are expected for ILs with longer alkyl-chain and larger anions. Both samples were fully deuterated to observe coherent scattering from the atoms forming the ions.

Figure 2 shows the neutron diffraction data of C8mimPF$_6$. Two clear peaks appeared at 1.0 Å^{-1} and 0.3 Å^{-1}. From the previous X-ray and neutron diffraction data and also computer simulation data, the former peak may be due to the correlation between the ions and the latter due to the correlation between the domains. On cooling, the ionic peak slightly shifted to the high-Q side, while the intensity of the domain peak drastically increased. It is of interest that the peak intensity still increases even below the glass transition temperature T_g as shown in the inset of Fig. 2. This result indicates that the atoms forming domains are still fluctuating even below T_g. Similar data were obtained also for C8mimTFSI.

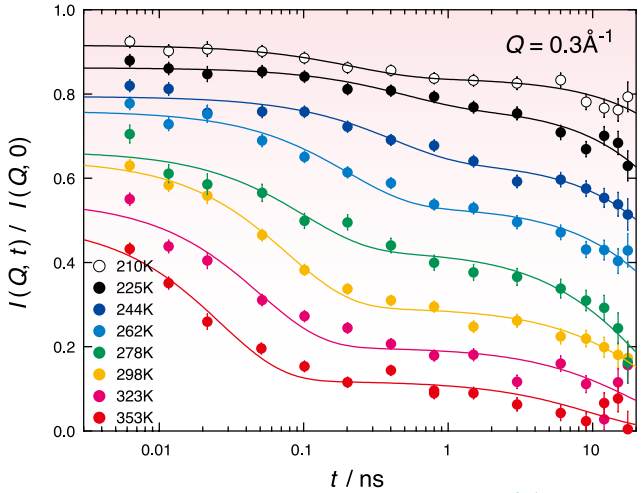

Fig. 3. NSE data of C8mimPF$_6$ at Q = 0.3 Å^{-1}.

Figure 3 shows the NSE data, intermediate scattering functions, of C8mimPF$_6$ at Q = 0.3 Å^{-1}. The data are fitted well to two exponential functions, corresponding to slower and faster relaxations, with two adjustable prefactors. It is noteworthy that, on cooling the sample, the fraction of the slower relaxation becomes larger while that of the faster relaxation smaller. Taking the diffraction data described above into consideration, the slower relaxation originates from the domains and the faster one from some sort of broken domains. This is the first experimental data demonstrating the relaxation of the domains. We are now planning the NSE experiment using neutrons with the wavelength 10 Å to extend the time region up to 50 ns. Then, clear relaxation data will be obtained at lower temperatures. The temperature dependence of the domain relaxation will give important information to clarify the mechanism of the domain formation in ILs.

Authors
O. Yamamuro, M. Kofu, T. Ueki, M. Watanabe[a], and M. Nagao[b]
[a]Yokohama National University
[b]National Institute of Standards and Technology and Indiana University (USA)

Novel Magnetic State in Ferromagnetic Frustrated Chain LiCuVO$_4$

Masuda Group

One of the recent interests in condensed matter science is to search for a spin liquid that exhibits order not in a conventional two-spin correlation but in other correlations such as magnetic multipole or spin chirality. A 1D frustrated spin chain with a ferromagnetic nearest-neighbor interaction (J_1) and an antiferromagnetic next-nearest-neighbor interaction (J_2) is diversity of such novel states. In zero field vector spin chirality does order with a broken Z_2 symmetry [1]. At a field close to the ferromagnetic polarized phase, a pair of magnons form a bound state [2], and its Bose condensation at approximately $q = \pi$ induces the quasi-long-range order of transverse spin nematic correlation $\langle S_0^+ S_1^+ S_l^- S_{l+1}^- \rangle$ [3]. At the same time longitudinal two spin correlation exhibits spin density wave like sinusoidal behavior; $\langle S_0^z S_l^z \rangle \sim A_z \cos(2k_f l)/l|l|^\eta$ [4]. Here $2k_f$ is the density of two-magnons. In real magnet, weak interchain interaction induces magnetic long-range order (LRO) at low temperatures but the LRO would inherit quantum nature. In the case of the vector chiral (VC) phase, a spiral order in which the magnitude of the magnetic moment is strongly suppressed owing to quantum fluctuation would be induced. In the case of nematic state, the LRO of the longitudinal spin correlation would appear with the propagating wave vector $2k_F$ in reasonably high field region.

LiCuVO$_4$ is a candidate compound for 1D ferromagnetic frustrated system. At low temperature interchain interaction induces a spiral magnetic LRO in the *ab*-plane with a propagation vector k_{sp} = (0 0.532 0) at zero and low magnetic

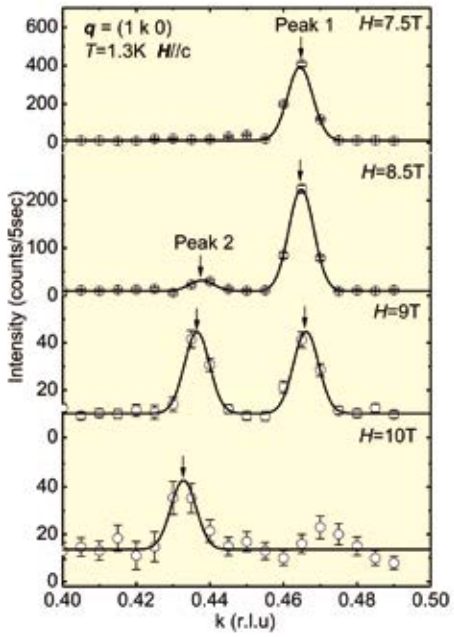

Fig. 1. Neutron diffraction profile at **q** = (1 *k* 0) in H k c at *T* = 1.3 K. Peak 1 is from the *ab*-plane spiral structure and peak 2 is from the spin density wave structure.

field [5]. Magnetic excitation measured by inelastic neutron scattering experiment was explained by spin wave calculation based on ferromagnetic frustrated chain with J_1 = -1.6 meV, J_2 = 3.56 meV, and J_{inter} = -0.4meV [6]. The realized spin model is a weakly coupled ferromagnetic frustrated chain with a NNN AF interaction. Hence the observed spiral order in zero and low field is ascribed to the development of two spin correlation in the theoretically predicted VC order in the isolated chain. Applying high field would induce nematic-like state that is characterized by the longitudinal SDW with field dependent propagation vector. Indeed unknown high field phase was reported at $H > 8$ T. Here we report neutron diffraction study to reveal the nature of the new high field phase in $LiCuVO_4$ [7].

Magnetic field dependence of neutron diffraction profiles at **q** = (1 *k* 0) ($0 \le k \le 1$) are collected at $T = 1.3$ K as shown in Fig. 1. At $H = 7.5$ T, a peak (peak 1) is observed at $k \sim 0.465$, which coincides with zero field data. With increasing field, peak 1 is suppressed and a new peak (peak 2) appears at $k \sim 0.438$ at 8.5 T. In addition, the intensity of peak 2 increases and its position changes. The field dependence of the peak positions are summarized in Fig. 2. The wave vector of peak 1 is constant and the *ab* spiral magnetic structure

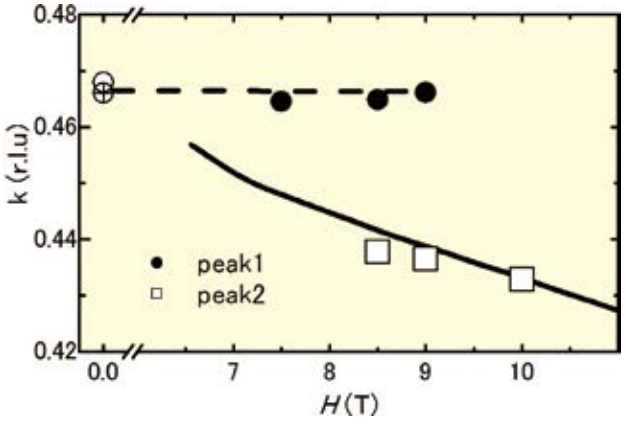

Fig. 2. Magnetic field dependence of Bragg peak position

persists up to $H \sim 9$ T. The wave vector of peak 2 monotonically decreases with H. Solid curve is the field dependence of the characteristic vector $2k_F$ of the nematic state that is theoretically calculated and the data is reasonably reproduced by the theory. Thus the high field phase in $LiCuVO_4$ is identified as the long-range order of the longitudinal sinusoidal spin correlation originally predicted in an isolated ferromagnetic frustrated chain.

References
[1] A. Kolezhuk and T. Vekua, Phys. Rev. B **72**, 094424 (2005).
[2] A.V. Chubkov, Phys. Rev. B **44**, 4693 (1991).
[3] L. Kecke, T. Momoi, and A. Furusaki, Phys. Rev. B **76**, 060407 (2007) .
[4] T. Hikihara, L. Kecke, T. Momoi, and A. Furusaki, Phys. Rev. B **78**, 144404 (2008).
[5] B.J. Gibson *et al*., Physica B **350**, e253 (2004).
[6] M. Enderle *et al*., Europhys. Lett. **70**, 237 (2005).
[7] T. Masuda, M. Hagihala, Y. Kondoh, K. Kaneko, and N. Metoki, J. Phys. Soc. Jpn. **80**, 113705 (2011).

Authors
T. Masuda, M. Hagihala, Y. Kondoh[a], K. Kaneko[b], and N. Metoki[b],
[a]Yokohama city university
[b]Japan Atomic Energy Agency

Ultra-High Magnetic Field Precision Magnetization in the Vertical Single-Turn Coil System

Takeyama, Y. Matsuda, and Tokunaga Groups

Magnetization is one of the most important measurements for understanding electro-magnetic properties of materials. Utilizing time variation of the magnetic flux inherent to a pulse magnet, the electromagnetic induction method is mostly used as a tool for a sensitive magnetization measurement in a variety of magnetic materials. In recent years, there occurred high demands for magnetization measurements in very high magnetic fields. On the other hand, a magnetic field above 100 T is only generated in a destructive manner, i.e., by destroying the magnet. The single-turn coil (STC) technique is very useful for solid-state physics measurements in a range of ultra-high magnetic fields of up to 300 T, since the coil only explodes outwards, while the sample and the equipment that holds it are usually kept intact inside the exploding coil, and both the elevating and descending of the magnetic field is utilized in a one-shot measurement. A peak field of up to 200 T can be generated in a 10-mm bore of the coil by an injection of mega-ampere from 200 kJ fast operating capacitor banks installed at the International MegaGauss Science Laboratory ISSP [1].

First application of the pickup coil detection of the magnetization to the STC technique was conducted by S. Takeyama and K. Amaya, who obtained the magnetization curve of $CsCoCl_3$ in magnetic fields up to 90 T at a temperature 4.2 K [2]. This direction of research has been continued, with further technical improvement achieved by T. Goto *et al*. to obtain a nice magnetization curve of a typical itinerant ferro-magnet YCo_3 up to 110 T. At Humboldt University in Berlin, A. Kriste *et al*. have achieved compensation ratios of better than 10^{-3} in two alternatively wound parallel pickup coils. In addition, magnetization measurement in magnetic fields of up to 130 T was applied to bismuth-based manganites ($Bi_{0.5}$ Ca $_{0.5}MnO_3$, $Bi_{0.5}$ Sr $_{0.5}MnO_3$) in order to

investigate the nature of the ferromagnetic phase in terms of its relevance to the charge order phase [3]. All of these, however, are such that the signal-to-noise ratio and the level of the background signal were insufficient to provide details of the absolute values of magnetization, *M*, in magnetic fields, and were only sufficient to determine the transition points of a magnetic field from *dM/dt*.

We have established a precision magnetization measurement system in a vertical-STC, with approaching comparable data quality obtained by the nondestructive long pulse magnet. Due to the deformation of the coil during the explosive outward movement of the magnet coil, the time dependences of the magnetic field distribution inside the coil were carefully examined, and the best position of the twin-parallel pick-coils were identified. Schematics of the magnetic probe and its component are presented in Fig.1. The magnetic pickup coils are positioned precisely at the center of the single-turn coil. A cryostat was specifically designed for the V-STC system as shown in Fig.1 (a,b). The upper part of the cryostat is made of stainless steel, and is comprised of a liquid He container with a tail section made of glass epoxy (Fiber-Reinforced Plastic; FRP) thin tubes. The thickness of the tube walls is 0.7 mm for both the innermost and the outermost walls, and 0.5 mm for the other two walls. Thus, the spaces of the inner vacuum insulating layer, the liquid N_2 layer, and the outer vacuum insulating layer are designed to be 0.3 mm, 0.5 mm and 0.5 mm, respectively. The FRP thin tubes are connected smoothly to the upper stainless steel tubes by a cryogenic epoxy adhesive (Nitofix, SK-229). Liquid He stored at the container of 0.3 ℓ was maintained for more than 3 hours.

Our new system has been applied to a geometrically frustrated magnets which have been one of an current issue of topics as its ground state are macroscopically degenerated and are vulnerable to small perturbations (spin-lattice interaction, quantum and thermal fluctuation, etc.). Application of magnetic field causes the appearance of peculiar magnetic phenomena such as the magnetization plateaus, magnetic supersolids and crystalline magnon states as a result of interplay between a magnetic field and frustrated spin exchange interaction. Among the numerous frustrated magnets, $CdCr_2O_4$ is recognized as one of the typical three-dimensional frustrated magnets exhibiting a very high Curie-Weiss temperature and a low Neel temperature (T_N/Θ_{CW}=8 K/70 K ~ 0.1 «1), which is caused by suppression of a magnetic order by the geometrical frustration, which requires multiple extreme physical conditions, such as ultra-high magnetic fields and very low temperatures, for thorough understanding of the magnetic orders. H. Ueda *et al*. reported magnetization of $CdCr_2O_4$ in magnetic fields up to 50 T using nondestructive long pulse magnets [4]. They found a first-order phase transition at 28 T followed by a wide magnetization plateau with a half-of-full moment (1/2 plateau). After this, H. Mitamura *et al*. have attempted measurements in magnetic fields up to 80 T by the induction method in the STC at 6 K. They could have shown a second order phase transition at 61 T and a first order phase transition at 77 T inferred only from data of the descending magnetic field of *dM/dt*. Signals from data of elevating magnetic field were difficult to analyze due to large ignition noises. Lately, Kojima *et al*. have applied a Faraday rotation method to this material for evaluation of magnetization [5]. They have carried out systematic measurements in wide temperatures in magnetic fields up to 140 T by the STC, and the magnetization processes until its full saturation moment are thoroughly revealed in wide range of temperature.

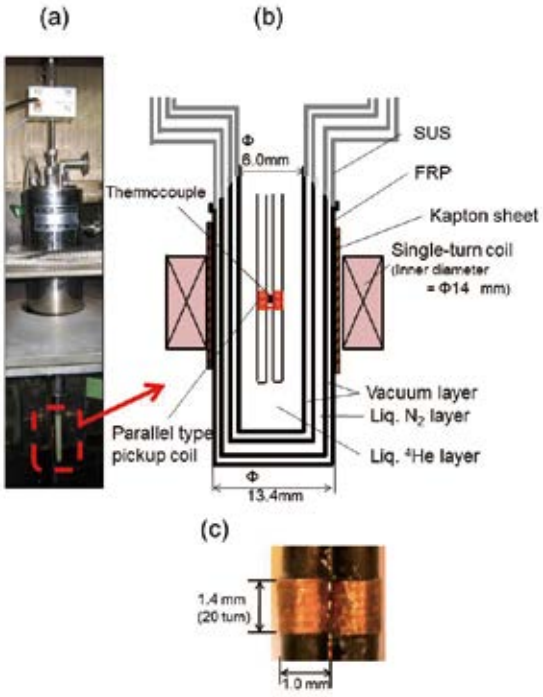

Fig. 1. (a) Photo picture of the cryogenic container developed for the vertical-STC, and (b) cross-sectional diagram of the tail section with (c) a photo picture of the self-compensated magnetic pickup coils.

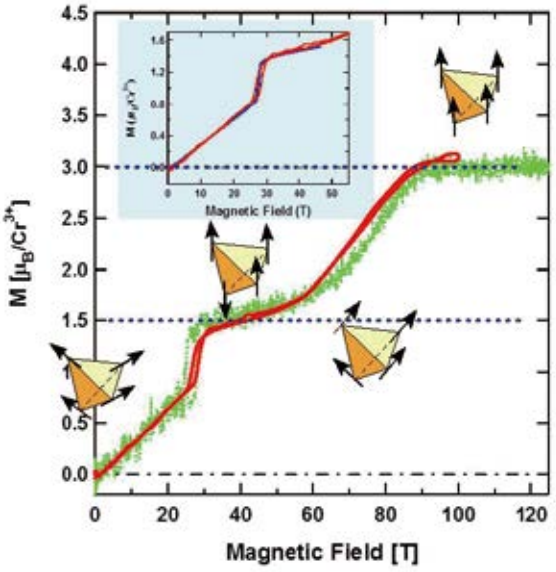

Fig. 2. The magnetization data measured up to 103 T at 4.2 K with elevating and descending magnetic field (red lines), together with the data taken from the Faraday rotation previously measured at 7 K (green plots) [5]. Spin moment configuration in each magnetic phase is shown. The inset is the comparison with those taken by a non-destructive long pulse magnet measured at 4.2 K (blue lines).

The results of the magnetization data measured up to 103 T with elevating and descending magnetic field are presented in Fig. 2 together with the data taken from the Faraday rotation previously measured at 7 K [5]. Both data coincide well with each other within the error of 3 % with respect to the full saturation moment. In the inset, the data is also compared with those measured by the long-pulse magnet in magnetic fields of up to 55 T. Owing to slow rate of the flux change subjected to the long-pulse magnet, a width of the hysteresis is almost invisible in this figure, but the transition occurred at a midpoint in magnetic fields between the hysteresis observed in the data taken by the present measurement. Striking coincidence is obtained in the two data. All the details are described in reference [6].

References
[1] N. Miura, T. Osada, and S. Takeyama, J. Low Temp. Phys. **133**, 139 (2003).
[2] S. Takeyama *et al.,* J. Phys. E **21**, 1025 (1988); K. Amaya *et al.*, Physica B**155**, 396 (1989).
[3] A. Kirste *et al.,* Phys. Rev. B **67**, 134413 (2003).
[4] H. Ueda *et al.*, Phys. Rev. Lett. **94**, 047202 (2005)
[5] E. Kojima *et al.*, Phys. Rev. B **77**, 212408 (2008).
[6] S. Takeyama, R. Sakakura, Y. H. Matsuda, A. Miyata, and M. Tokunaga, J. Phys. Soc. Jpn. **81**, 014702 (2012).

Authors
S. Takeyama, Y. H. Matsuda, A. Miyata, and M. Tokunaga

Magnetic Phases in Geometrically Frustrated Magnet, $ZnCr_2O_4$, Revealed by Ultra-High Magnetic Fields Up to 600 T

Takeyama Group

Chromium spinel oxides, ACr_2O_4 (A = Zn, Cd, Hg), in which Cr^{3+} ions form a pyrochlore lattice are regarded as three-dimensional geometrically frustrated magnets. In these compounds, a spin-lattice coupling plays a crucial role to cause the emergence of diverse magnetic phases with simultaneous lattice distortion under magnetic fields. Interestingly, our recent studies exhibited existence of an unusual magnetic structure (a canted 2:1:1 magnetic structure) at lower magnetic field side of a 1/2 plateau phase only in $ZnCr_2O_4$, compared with $HgCr_2O_4$ and $CdCr_2O_4$ [1]. This is because a spin-lattice coupling of $ZnCr_2O_4$ places in a small limit. In this light, elucidation of magnetic phases in $ZnCr_2O_4$ up to a saturated magnetization moment has been highly demanded. However, full-magnetization processes of $ZnCr_2O_4$ can never be observed unless we overcome difficulties to achieve the multiple extreme conditions, ultra-high magnetic fields in the range of several hundred Tesla and very low temperature down to a few Kelvin. We have developed an original hand-made miniature liquid-He flow-type cryostat made totally of a "Stycast" resin and a cryogenic system for the electro-magnetic flux compression (EMFC) method as shown in Fig. 1, which have enabled us to conduct magneto-optical measurements at cryogenic temperatures of down to 4.6 K and under extremely high magnetic fields of up to 600 T [2].

The magnetization processes of $ZnCr_2O_4$ up to a full saturation moment were unveiled by the precise Faraday rotation (FR) measured up to 600 T and at 4.6 K, of which typical data are shown in Fig. 2 (a). In addition, we could

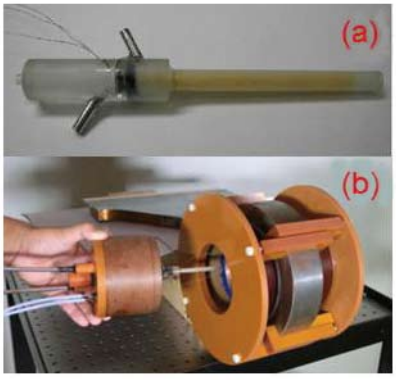

Fig. 1. (a) Photo picture of a hand-made miniature liquid-He flow-type cryostat made totally of a "Stycast" resin, and (b) photo picture of a total cryogenic system set to a primary coil for the EMFC method.

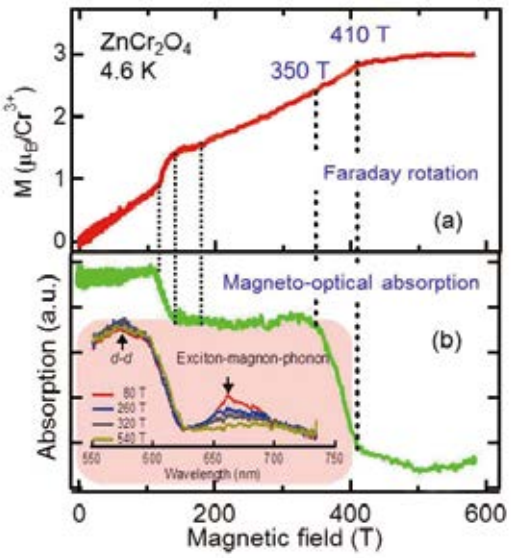

Fig. 2. (a) The magnetization curve evaluated from the FR of $ZnCr_2O_4$ in magnetic fields up to 600 T and at temperature 4.6 K, and (b) the optical absorption intensity of the incident laser used for the FR measurements as a function of magnetic field. The dotted line shows a magnetic field at which an anomaly occurred in the absorption intensity. The inset shows magneto-optical absorption spectra around the energy at which the EMP and intra-d-d transitions take place in magnetic fields of up to 540 T and at 12 K.

also obtain an optical absorption intensity of $ZnCr_2O_4$ as a function of magnetic field in the signal of the Faraday rotation as shown in Fig. 2 (b). A ferromagnetic phase transition was observed at 410 T and 4.6 K, above which magnetization of $ZnCr_2O_4$ was saturated at a value of 3 μ_B/Cr^{3+}. In addition, an abrupt change in FR absorption intensity (a green line in Fig.2 (b)) was found at 350 T, while the magnetization monotonically increased. In order to clarify this anomaly, magneto-optical absorption spectral measurements were carried out by a streak spectroscopy as shown in the inset of Fig. 2 (b). As a result, anomalies of the optical absorption intensity were observed in both the intra-*d* band and the exciton-magnon-phonon transitions, in which the spectral shape and the peak position are very susceptible to the crystal and the magnetic structure. This anomaly indicates definite existence of a novel magnetic phase accompanied by changes of both crystal and magnetic structure. This new phase is beyond the prediction of the theory taking account of the spin-lattice coupling developed by Penc *et al.* [3]. The most feasible phase is realization of an umbrella-like magnetic structure between the canted 3:1 and the ferromagnetic phase.

If we assume the new phase as the umbrella-like spin alignment, then there found an interesting analogy with the theory developed for the quantum phases in ^{4}He by Matsuda and Tsuneto [4], and Liu and Fisher [5]. According to their theories, the supersolid phase is sandwiched by a solid and

Magnetic phase ($ZnCr_2O_4$)	Antiferro-magnetic	Canted 2:1:1	1/2 plateau	Canted 3:1	Umbrella ?	Ferromagnetic
Magnetic structure						
^{4}He	Superfluid	Supersolid	Solid	Supersolid	Superfluid	Liquid

Table 1. Physical analogy between magnetic phases of $ZnCr_2O_4$ and the theory developed for the quantum phases of ^{4}He.

a superfluid phase, and is unlikely to be adjacent to a liquid phase because a liquid-supersolid transition takes place by a simultaneous breaking of both the translational and spins rotational symmetry. Therefore, our proposed magnetic phases agree quite well with the sequence of phases; the canted 3:1 phase (i.e., supersolid) is sandwiched by the 1/2 plateau phase (i.e., solid phase) and the umbrella-like magnetic structure (i.e., superfluid phase). This analogy is well demonstrated in Table 1, presenting a beautiful and symmetric correspondence.

References

[1] A. Miyata *et al*., J. Phys. Soc. Jpn. **80**, 074709 (2011).
[2] A. Miyata, *et al*. , Phys. Rev. Lett. **107**, 207203 (2011).
[3] K. Penc *et al*., Phys. Rev. Lett. **93**, 197203 (2004).
[4] H. Matsuda and T. Tsuneto, Prog. Theor. Phys. Suppl. **46**, 411 (1970).
[5] K. S. Liu and M. E. Fisher, J. Low Temp. Phys. **10**, 655 (1973).

Authors

A. Miyata and S. Takeyama

Field-Induced Melting of Spin and Orbital Order in Sulfur-Doped Iron-Telluride

Tokunaga Group

Since 2008, iron-based superconductors have attracted considerable attention because of the occurrence of high temperature superconductivity in the vicinity of antiferromagnetic order similar to the cuprate superconductors [1]. The superconductivity in the cuprates emerges when antiferromagnetic states of the parent compounds are removed by chemical substitution, whereas that in the ironates can be induced also by application of pressure to the antiferromagnetic states. Therefore, it is naively interesting to study what happens if we can remove the antiferromagnetism in the parent compounds by application of magnetic fields. As far as we know, there is little challenge to suppress the antiferromagnetism by magnetic fields in this class of materials [2].

We studied physical properties of $Fe_{1+y}Te_{1-x}S_x$ (x = 0, 0.05, and 0.10) in high magnetic fields. Since these materials have relatively low Néel temperatures (T_N) among

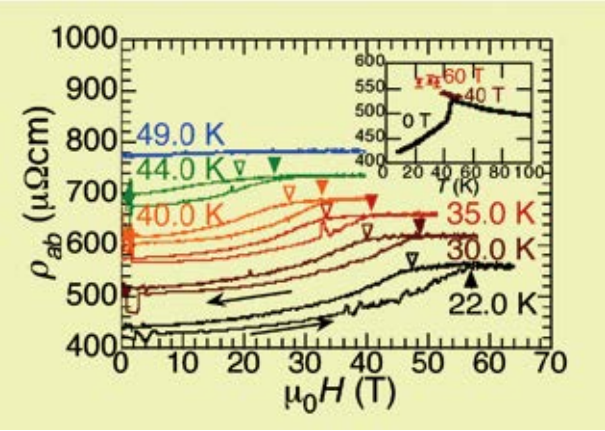

Fig. 1. Longitudinal magnetoresistance of the $Fe_{1+y}Te_{1-x}S_x$ crystal with nominal x = 0.10. The data were vertically offset for clarity. The positive magnetoresistance effects with prominent hystereses indicate the occurrence of first-order transitions from the antiferromagnetic state in zero field. The inset shows temperature dependence of the in-plane resistivity at $\mu_0 H$ = 0 T, 40 T, and 60 T. The resistivity in the high-field phase falls on the line extrapolated from that in the paramagnetic state in zero field indicating the melting of the spin order in the high-field phase.

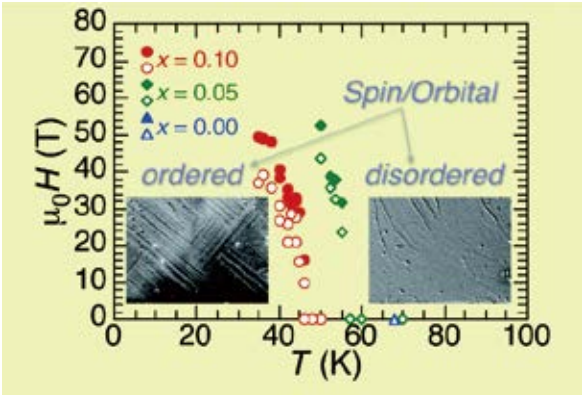

Fig. 2. Field-temperature phase diagram of $Fe_{1+y}Te_{1-x}S_x$ for $H \parallel c$-axis. The insets show the polarizing microscope images on the cleaved ab-plane surfaces of an x = 0.05 crystal. The stripe-like structure in the low temperature phase (left inset) represents the twin domains caused by the orbital order. Application of high magnetic field wiped out these stripe-like structures representing the field-induced melting of the orbital order [4].

the ironates, we expect prominent effects of magnetic fields within our pulsed fields up to 65 T. The spin order in the iron-telluride is mysterious because the Fermi-surface nesting scenario, which can explain the stripe-type spin order found in most of the parent compounds of the ironate superconductors, cannot account for the bicollinear spin order in this compound. Since this spin order is accompanied by the ordering of the 3d orbitals in the iron ions, the correlation between these two ordering can play the key role to realize the unique antiferromagnetic state [3].

In zero fields, these crystals show steep decrease in resistance upon cooling below T_N as shown in the inset of Fig. 1. Application of high magnetic fields to these antiferromagnetic states causes steep increases in resistance to the values extrapolated from those in the paramagnetic states, indicating the field-induced melting of the spin order (Fig. 1). The orbital order can be detected by direct observation of the sample surface because the violation of the four-fold symmetry within the ab-plane appears as the stripe-like twin structures in the polarizing microscope images as shown in the insets of Fig. 2. With using a high-speed camera, we captured the changes in polarizing microscope images in pulsed high magnetic fields across the phase boundary shown in Fig. 2. The obtained images visually demonstrate the collapse of the orbital order simultaneously with the melting of the spin order. Our results indicate the importance of the cross correlation between spin and lattice/orbital degrees of freedom in these compounds [4]. To study the ground states of the spin/orbital disordered states in this compounds, experiment in higher fields are in progress.

References

[1] Y. Kamihara, T. Watanabe, M. Hirano, and H. Hosono, J. Am. Chem. Soc. **130**, 3296 (2008).
[2] M. Tokunaga, I. Katakura, N. Katayama, and K. Ohgushi, J. Low Temp. Phys. **159**, 601 (2010).
[3] A. M. Turner, F. Wang, and A. Vishwanath, Phys. Rev. B **80**, 224504 (2009).
[4] M. Tokunaga, T. Kihara, Y. Mizuguchi, and Y. Takano, J. Phys. Soc. Jpn. **81**, 063703 (2012).

Authors

M. Tokunaga, K. Kihara, Y. Mizuguchi[a], and Y. Takano[b]
[a]Tokyo Metropolitan University
[b]The National Institute for Materials Science

Partial Kondo Breakdown in $CeRu_2Si_2$ at High Magnetic Fields

Y. Matsuda Group

Most of the heavy fermion (HF) systems contain Ce or Yb. The occupation number of the 4*f* electron in the orbital (n_f) is close to 1 for Ce, and in Yb, the occupation number of the 4*f* hole (n_h) is close to 1. The 4*f* electrons acquire an itinerant character because of the strong hybridization with the conduction electrons. The energy level of the correlated 4*f* electrons is near the Fermi energy, because the significant electron-electron many-body interaction causes the electrons to become itinerant HFs. The degree of the itinerancy is determined by the strength of the electron interaction. The itinerant character manifests itself in the deviation of the occupation number of the *f* electron or hole from unity: n_f or n_h. In HF systems, $1 - n_f$ ($1 - n_h$) must be very small but finite, indicating that the electrons are highly localized and only slightly itinerant.

The valence state of Ce in a canonical heavy fermion compound $CeRu_2Si_2$ has been investigated by synchrotron X-ray absorption spectroscopy at 1.8 K in high magnetic fields of up to 40 T. It was found that the valence was slightly larger than for the pure trivalent state (Ce^{3+}: f^1), as expected in heavy fermion compounds, and it decreased toward the trivalent state as the magnetic field was increased.

In Figure 1 (a), the valence is plotted as a function of magnetic field, and the magnetization (*M*) and its magnetic field derivative (*dM/dH*) at 4.2 K are shown as a function of the magnetic field in Fig.1 (b) for comparison. In the *M* and *dM/dH* curves, the metamagnetic transition is clearly visible at the transition field of 8 T (H_m). An unusual magnetic field dependence of the valence was found in the field variation of the valence. The valence decreased slightly in low magnetic fields and the rate of the decrease was larger when the magnetic field was higher than about 8 T; this magnetic field was defined as H_v. It was clear that H_v corresponded to the metamagnetic transition field, H_m. The valence gradually decreased and continued to change even at magnetic fields higher than H_m. The valence decreased even at 40 T, although the metamagnetic transition was probably complete above 20 T.

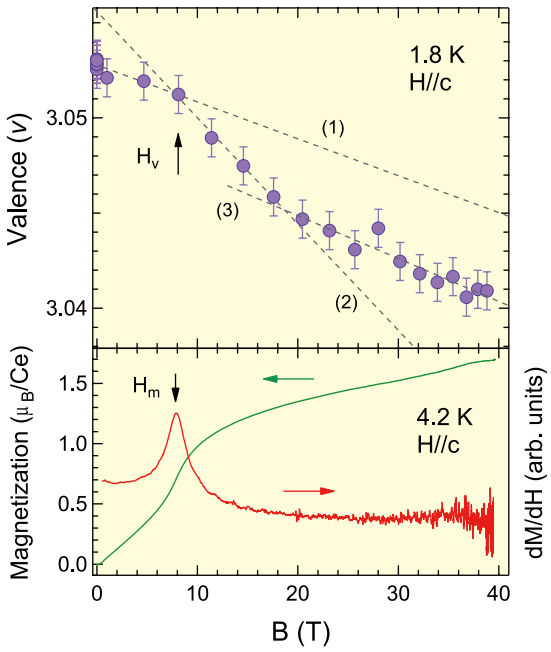

Fig. 1. (a) Magnetic field dependence of the Ce valence at 1.8 K. The dashed lines (1), (2) and (3) show the slope of the valence change in low, medium and high magnetic field ranges, respectively. The arrow denotes the characteristic magnetic field H_v for the valence change (b) Magnetic field dependence of the magnetization (*M*) and the field derivative (*dM/dH*) at 4.2 K. The arrow denotes the metamagnetic transition field H_m.

If a complete field-induced valence transition takes place, Δn_f /1-n_f should be close to 1.0. It is actually about 0.7 in the Yb-based heavy fermion compound, $YbAgCu_4$. [1] The value of Δn_f /1-n_f obtained in the present work is 0.012 / 0.053 ~ 0.23, suggesting that the itinerancy of the *f* electrons is suppressed but the *f* electrons were still in far from the complete Kondo breakdown even at the 40-T magnetic fields.

Reference

[1] Y. H. Matsuda, T. Nakamura, J. L. Her, K. Kindo, S. Michimura, T. Inami, M. Mizumaki, N. Kawamura, M. Suzuki, B. Chen, H. Ohta, and K. Yoshimura, J. Phys. Soc. Jpn. **81**, 015002 (2012).

Authors

Y. H. Matsuda, T. Nakamura, J. L. Her, S. Michimura[a], T. Inami[a], and T. Ebihara[b]

[a]Japan Atomic Energy Agency

[b]T. Shizuoka University